

## Distinguishing Kerr naked singularities and black holes using the spin precession of a test gyro in strong gravitational fields

Chandrachur Chakraborty,<sup>1,\*</sup> Prashant Kocherlakota,<sup>1,†</sup> Mandar Patil,<sup>2,‡</sup> Sudip Bhattacharyya,<sup>1,§</sup>  
Pankaj S. Joshi,<sup>1,||</sup> and Andrzej Królak<sup>2,¶</sup>

<sup>1</sup>Tata Institute of Fundamental Research, Mumbai 400005, India

<sup>2</sup>Institute of Mathematics of Polish Academy of Sciences, Sniadeckich 8, 00-956 Warsaw, Poland

(Received 2 December 2016; published 12 April 2017)

We study here the precession of the spin of a test gyroscope attached to a stationary observer in the Kerr spacetime, specifically, to distinguish a naked singularity (NS) from a black hole (BH). It was shown recently that for gyros attached to static observers, their precession frequency became arbitrarily large in the limit of approach to the ergosurface. For gyros attached to stationary observers that move with nonzero angular velocity  $\Omega$ , this divergence at the ergosurface can be avoided. Specifically, for such gyros, the precession frequencies diverge on the event horizon of a BH, but are finite and regular for a NS everywhere except at the singularity itself. Therefore a genuine detection of the event horizon becomes possible in this case. We also show that for a near-extremal NS ( $1 < a_* < 1.1$ ), characteristic features appear in the radial profiles of the precession frequency, using which we can further distinguish a near-extremal NS from a BH, or even from a NS with larger angular momentum. We then investigate the Lense-Thirring (LT) precession or nodal plane precession frequency of the accretion disk around a BH and NS to show that clear distinctions exist for these configurations in terms of radial variation features. The LT precession in equatorial circular orbits increases on approaching a BH, whereas for NS it increases, attains a peak, and then decreases. Interestingly, for  $a_* = 1.089$ , it decreases until it vanishes at a certain radius, and it acquires negative values for  $a_* > 1.089$  for a certain range of  $r$ . For  $1 < a_* < 1.089$ , a peak appears, but the LT frequency remains positive definite. There are important differences in accretion disk LT frequencies for a BH and a NS and since LT frequencies are intimately related to observed quasiperiodic oscillations, these features might allow us to determine whether a given rotating compact astrophysical object is a BH or a NS.

DOI: [10.1103/PhysRevD.95.084024](https://doi.org/10.1103/PhysRevD.95.084024)

### I. INTRODUCTION

An important issue in relativistic astrophysics and gravitation theory today has been to rule out the existence of naked singularities in the gravitational collapse of massive matter clouds. Alternatively, if naked singularities (NSs) do exist as end states of massive stars collapsing under self-gravity towards the end of their life cycles, the important physical question would then be, how can one decide whether a particular astrophysical compact object is a black hole (BH) or a NS? This is a key issue, very much at the heart of making physical predictions about very strong gravity regions in the Universe, which major astrophysical missions are probing currently [1].

In this connection, it is important to examine in some detail the Kerr geometry configurations and find physical quantities that can be used to differentiate a BH from a NS. The Kerr spacetime describes either a rotating BH or NS, depending on the Kerr spin parameter  $a$ , which is the

specific angular momentum ( $J/M$ ). The Kerr BH possesses two event horizons and two ergoregions which are the outer and inner event horizons and outer and inner ergoregions. The region between the outer event horizon and outer ergoradius is called the outer ergoregion or simply the ergoregion. Here, we will be primarily concerned with this region. Similarly, the region between the inner event horizon and the inner ergoradius is called the inner ergoregion. The inner ergoregion is often dismissed as being unphysical since we do not really know reliably what happens behind the outer event horizon of a rotating black hole. The rotational energy of the BH can be extracted by a particle from the outer ergoregion (henceforth, just ergoregion) and this is called the Penrose process.

The ergoregion is responsible for several interesting phenomena, one of which has recently been discussed in Ref. [2], where the exact Lense-Thirring (LT) precession frequency of a test gyroscope in Kerr spacetime was derived and it was shown that the LT precession frequency diverges on the boundary of the ergoregion (henceforth, “ergosurface”) of a BH. For BHs, the dimensionless Kerr parameter satisfies  $a_* = J/M^2 \leq 1$ . In another work [3], the spin precession frequency was discussed in detail in the case of a NS ( $a_* > 1$ ). For a NS, the entire region between the inner and outer ergo radii is defined to be the

\*chandrachur.chakraborty@tifr.res.in

†k.prashant@tifr.res.in

‡mpatil@impan.pl

§sudip@tifr.res.in

||psj@tifr.res.in

¶krolak@impan.pl

ergoregion. It was discussed there that the drastic change in geometry of the ergoregion for  $a_* > 1$ , as opposed to  $a_* \leq 1$ , could allow for a differentiation of the two spacetimes using a physical quantity, namely the precession frequency of gyroscopes attached to static observers placed around these compact objects. Specifically, for the NS configuration, along the pole a finite angle opens up where the ergoregion is absent and  $r = 0$  can be accessible via this region without passing through the ergoregion. This region broadens when values of  $a_*$  increase beyond 1 and the ergoregion shrinks toward the equator. It was discussed that the precession frequency always diverges on the ergosurface. Since the ergoregion completely bounds a BH, on approaching it in any direction, one would find a divergence. However, in the case of a NS, the frequency remains finite and regular in the opening angle due to the absence of the ergoregion. We find this to be a possible experiment to distinguish the two qualitatively distinct Kerr configurations.

It was discussed in Ref. [4] how a nonrotating black hole can be distinguished from a naked singularity. In this paper, we discuss how one can distinguish a rotating BH from a NS using the behavior of the precession frequency of the spin of a test gyro which moves, in general, along a nongeodesic orbit around such a Kerr compact object, thus generalizing the earlier work on distinguishing black holes from naked singularities. In this regard, we find it useful to mention that Bini *et al.* recently analyzed the precession of a test gyroscope along bound [5] and unbound [6] equatorial plane geodesic orbits around a BH with respect to a static reference frame whose axes point towards “fixed stars.” It is well known that the paths followed by spinning test particles are not, in general, geodesics [7,8].

In the present article, we discuss the precession of a gyroscope both outside and inside the ergoregion of a BH and a NS. We find that the divergence of the spin precession frequency on the ergosurface reported in Ref. [3] can be avoided if the test gyro moves with a nonzero angular velocity  $\Omega$ . In Ref. [3], the motivation was to study the precession of spins of gyroscopes attached to stationary observers, that is, to answer physical questions like how the gyroscope of an astronaut holding his spaceship at a constant distance from a Kerr compact object will behave. The four-velocity ( $u$ ) of “static gyros” on the ergosurface satisfies  $u \cdot u = 0$ ; that is, it becomes null. However, if one introduces an azimuthal component to the four-velocity, the norm can be made nonzero and timelike. We can therefore extend the study of the behavior of a gyro into the ergoregion. We find that the precession frequency of the gyro behaves differently inside the ergoregion of a BH versus that of a NS, due to the presence of the event horizon, therefore rendering it a viable physical quantity that can be used to distinguish a BH from a NS.

We note that the Killing vectors of the Kerr spacetime provide invariant characterizations of the ergosurfaces and

horizons. The time translation Killing vector  $\partial_0$  is the unique Killing vector that approaches a unit timelike vector at spatial infinity and its vanishing norm gives the invariant location of the ergosurface. Further, one can construct a Killing vector from a linear combination, with constant coefficients, of  $\partial_0$  and the azimuthal Killing vector  $\partial_\phi$ . The vanishing norm of this Killing vector, for some fixed  $\Omega$  (say  $\Omega = \Omega_H$ ), can be used to invariantly determine the location of the horizon. With this motivation, we consider here the precession of the spin of gyroscopes attached to stationary observers, whose velocity vectors are proportional to the Killing vectors  $K = \partial_0 + \Omega\partial_\phi$ . These gyroscopes move along circular orbits around the central compact object with a constant angular velocity  $\Omega$ , which at any given  $(r, \theta)$  can be chosen to be in a particular range, so that  $K$  is timelike. Indeed, when the spacetime describes a BH, this frequency becomes arbitrarily large for observers located infinitesimally close to the horizon, in all coordinates. We interpret this as a coordinate invariant method to locate the horizon. For a NS, a divergence in the precession frequency occurs at the singularity itself, which is present in the equatorial plane. In [3], the precession frequency of gyroscopes attached to static observers was considered, namely, observers that do not change their spatial position with time. The velocity vectors of these observers are proportional to  $\partial_0$  and we found that the precession frequency for static observers located infinitesimally close to the ergosurface became arbitrarily large, in all coordinates, thus invariantly indicating the location of the ergosurface.

In a later section, we examine the Lense-Thirring precession frequency and the fundamental frequencies of an accretion disk around a Kerr compact object as the other distinguishing criterion of a NS from a BH. Stable circular orbits in the equatorial plane for both the BH and NS cases are investigated, and we show that there are important characteristic differences which can be used to distinguish the BH and NS configurations from each other. Specifically, we find the features of stable circular orbits in the equatorial plane for both the BH and NS cases. We also show that the radial and epicyclic frequencies show rather distinct features in the BH and NS cases. Further, in observed quasiperiodic oscillations (QPOs) from accretion disks, if one finds a clear peak at some radius, then the existence of NSs could possibly be established.

The scheme of the paper is as follows. In Sec. II, we discuss stationary observers. We outline the derivation for the spin precession frequency of a test gyro which rotates with a nonzero angular velocity in a general stationary and axisymmetric spacetime in Sec. III. We use this expression for the precession frequency specifically for the Kerr spacetime and discuss its features in various useful regimes of the spacetime in Sec. IV. Characteristic features of the precession frequency of a gyroscope orbiting NSs and BHs that can be used to distinguish them, in principle, are described in Sec. V. Further, in Sec. VI, features which can

be used to distinguish near-extremal NSs from NSs with higher angular momentum are discussed. In Sec. VII, we use the Lense-Thirring precession (orbital plane precession) of an accretion disk around a Kerr spacetime as another distinguishing criterion. We also discuss observational aspects related to QPOs. Finally Sec. VIII outlines our results and conclusions.

## II. STATIONARY OBSERVERS IN KERR SPACETIME

In a rotating spacetime, observers can remain still without changing their location with respect to infinity only outside the ergoregion. Such observers are called static observers [9,10] and their four-velocity is given as

$$u_{\text{static}}^{\sigma} = u_{\text{static}}^t (1, 0, 0, 0). \quad (1)$$

Once inside the ergoregion, it is impossible to stay fixed to a point without changing all three spatial coordinates (say,  $r, \theta, \phi$ ) of their world lines with time. The ergoregion is a characteristic feature of nonstatic stationary spacetimes. Specifically, in the case of the BH, its event horizon lies inside the ergoregion. This means that, in general, static observers cannot exist arbitrarily close to the horizon of a black hole. In contrast, an observer can hover very close to the horizon of a Schwarzschild black hole, remaining fixed. However, it is possible for observers to fix  $(r, \theta)$  and rotate (prograde only) around a BH or NS inside their ergoregion, with respect to infinity. Such observers are called stationary observers and their four-velocity is given as

$$u_{\text{statio}}^{\sigma} = u_{\text{statio}}^t (1, 0, 0, \Omega), \quad (2)$$

where  $t$  is the time coordinate and  $\Omega$  is the angular velocity of the observer. Since we are interested in studying timelike observers, the values that  $\Omega$  takes are restricted. This is true outside the ergoregion as well and retrograde rotating observers are then allowed. Let us henceforth call gyroscopes attached to static and stationary observers static gyroscopes and stationary gyroscopes, respectively, for brevity.

## III. SPIN PRECESSION OF A TEST GYROSCOPE: FORMALISM

Let us consider a test gyroscope attached to a stationary observer, which moves along a Killing trajectory in a stationary spacetime. The spin of such a gyroscope undergoes Fermi-Walker transport along

$$u = (-K^2)^{-\frac{1}{2}} K, \quad (3)$$

where  $K$  is the timelike Killing vector field. In this special situation, it is known that the gyroscope precession frequency coincides with the vorticity field associated with

the Killing congruence. That is, this gyroscope rotates relative to a corotating frame with an angular velocity and this effect is generally known as the ‘‘gravitomagnetic precession,’’ since the vorticity vector plays the role of a magnetic field in the 3 + 1 splitting of spacetime [11]. Thus, the general spin precession frequency of a test gyro,  $\Omega_s$ , is the rescaled vorticity field of the observer congruence and can be expressed as [10]

$$\begin{aligned} \tilde{\Omega}_s &= \frac{1}{2K^2} * (\tilde{K} \wedge d\tilde{K}) \\ \text{or, } (\Omega_s)_{\mu} &= \frac{1}{2K^2} \eta^{\lambda\beta\delta} K_{\lambda} \partial_{\beta} K_{\delta}, \end{aligned} \quad (4)$$

where  $\Omega_s$  is the spin precession frequency in the coordinate basis;  $*$  represents the Hodge star operator or Hodge dual;  $\eta^{\mu\lambda\beta\delta}$  represent the components of the volume form in spacetime; and  $\tilde{K}, \tilde{\Omega}_s$  are the one-forms of  $K$  and  $\Omega_s$ , respectively. In any stationary spacetime,  $K$  can be chosen to be  $K = \partial_0$  for which, from Eq. (4),  $\Omega_s$  becomes  $\Omega_{\text{LT}}$ , the LT precession frequency. This can be expressed as [2,10]

$$\Omega_{\text{LT}} = \frac{1}{2} \frac{\varepsilon_{ijkl}}{\sqrt{-g}} \left[ g_{0i,j} \left( \partial_l - \frac{g_{0l}}{g_{00}} \partial_0 \right) - \frac{g_{0i}}{g_{00}} g_{00,j} \partial_l \right]. \quad (5)$$

In a static spacetime, LT precession vanishes since  $g_{0i} = 0$ . On the other hand, it does not vanish in a stationary spacetime. Moreover, due to the presence of  $K^2 = g_{00}$  in the denominator, Eqs. (4) and (5) diverge if  $g_{00}$  vanishes. In a stationary and axisymmetric spacetime, this happens only on the ergosurface, which makes  $K$  a null vector there. Inside the ergoregion,  $K$  is no longer timelike but becomes spacelike. Thus, Eq. (5) is invalid inside the ergoregion as well as on its boundary.

Since the focal point of this paper is to study spin precession in the Kerr spacetime, we point out here that it has two Killing vectors: the time translation Killing vector  $\partial_0$  and the azimuthal Killing vector  $\partial_{\phi}$ . Any constant coefficient linear combination  $K = \partial_0 + \Omega \partial_{\phi}$  is also a Killing vector and this exhausts the set of Killing vectors in the Kerr spacetime. As stated earlier, the Killing vector  $\partial_0$  is the unique Killing vector that approaches a unit timelike vector at spatial infinity. We now consider the full timelike Killing vector of the Kerr spacetime and study spin precession for observers with  $u$ , that is, stationary observers. This is in contrast to [3], where the velocity was chosen to be proportional  $\partial_0$  and these described static observers. Therefore, for a general stationary spacetime which also possesses a spacelike Killing vector, we can write the most general timelike Killing vector as

$$K = \partial_0 + \Omega \partial_c, \quad (6)$$

where  $\partial_c$  is a spacelike Killing vector of that stationary spacetime and  $\Omega$ , for an observer moving along integral

curves of  $K$ , represents the angular velocity. The metric of this particular spacetime is independent of  $x^0$  and  $x^c$  coordinates. The corresponding covector of  $K$  is

$$\tilde{K} = g_{0\nu} dx^\nu + \Omega g_{\gamma c} dx^\gamma, \quad (7)$$

where  $\gamma, \nu = 0, c, 2, 3$  in four-dimensional spacetime. Separating space and time components, we can write  $\tilde{K}$  as

$$\begin{aligned} \tilde{K} &= (g_{00} dx^0 + g_{0c} dx^c + g_{0i} dx^i) \\ &+ \Omega (g_{0c} dx^0 + g_{cc} dx^c + g_{ic} dx^i), \end{aligned} \quad (8)$$

where  $i = 2, 3$ . Since we are mainly interested in the ergoregion of a stationary and axisymmetric spacetime, we can abolish  $g_{0i}$  and  $g_{ic}$  terms. Finally, we obtain

$$\tilde{K} = (g_{00} dx^0 + g_{0c} dx^c) + \Omega (g_{0c} dx^0 + g_{cc} dx^c) \quad (9)$$

and

$$\begin{aligned} d\tilde{K} &= (g_{00,k} dx^k \wedge dx^0 + g_{0c,k} dx^k \wedge dx^c) \\ &+ \Omega (g_{0c,k} dx^k \wedge dx^0 + g_{cc,k} dx^k \wedge dx^c). \end{aligned} \quad (10)$$

Now, Eq. (4) can be modified as

$$\tilde{\Omega}_p = \frac{1}{2K^2} * (\tilde{K} \wedge d\tilde{K}). \quad (11)$$

Substituting the expressions of  $\tilde{K}$  and  $d\tilde{K}$  in Eq. (11), we obtain the one-form of the precession frequency<sup>1</sup> as

$$\begin{aligned} \tilde{\Omega}_p &= \frac{\epsilon_{ckl} g_{l\mu} dx^\mu}{2\sqrt{-g}(1 + 2\Omega \frac{g_{0c}}{g_{00}} + \Omega^2 \frac{g_{cc}}{g_{00}})} \\ &\left[ \left( g_{0c,k} - \frac{g_{0c}}{g_{00}} g_{00,k} \right) + \Omega \left( g_{cc,k} - \frac{g_{cc}}{g_{00}} g_{00,k} \right) \right. \\ &\left. + \Omega^2 \left( \frac{g_{0c}}{g_{00}} g_{cc,k} - \frac{g_{cc}}{g_{00}} g_{0c,k} \right) \right], \end{aligned} \quad (12)$$

where we have used  $*(dx^0 \wedge dx^k \wedge dx^c) = \eta^{0kcl} g_{l\mu} dx^\mu = -\frac{1}{\sqrt{-g}} \epsilon_{kcl} g_{l\mu} dx^\mu$  and  $K^2 = g_{00} + 2\Omega g_{0c} + \Omega^2 g_{cc}$ . The corresponding vector ( $\Omega_p$ ) of the covector  $\tilde{\Omega}_p$  is

<sup>1</sup> $\Omega_p$  is not the LT precession frequency of the gyro. Since the gyro has a nonzero angular velocity  $\Omega$ , the precession frequency  $\Omega_p$  is modified. If we set  $\Omega = 0$ , we have  $\Omega_p = \Omega_{LT}$ . In this work, the expression of  $\Omega_p$  describes the overall precession, which includes the LT effect as well as some other effects (e.g., geodetic precession) which we will discuss as we proceed.

$$\begin{aligned} \Omega_p &= \frac{\epsilon_{ckl}}{2\sqrt{-g}(1 + 2\Omega \frac{g_{0c}}{g_{00}} + \Omega^2 \frac{g_{cc}}{g_{00}})} \\ &\left[ \left( g_{0c,k} - \frac{g_{0c}}{g_{00}} g_{00,k} \right) + \Omega \left( g_{cc,k} - \frac{g_{cc}}{g_{00}} g_{00,k} \right) \right. \\ &\left. + \Omega^2 \left( \frac{g_{0c}}{g_{00}} g_{cc,k} - \frac{g_{cc}}{g_{00}} g_{0c,k} \right) \right] \partial_l. \end{aligned} \quad (13)$$

In a stationary and axisymmetric spacetime with coordinates  $0, r, \theta, \phi$ , Eq. (13) reduces to

$$\begin{aligned} \tilde{\Omega}_p &= \frac{1}{2\sqrt{-g}(1 + 2\Omega \frac{g_{0\phi}}{g_{00}} + \Omega^2 \frac{g_{\phi\phi}}{g_{00}})} \\ &\left[ -\sqrt{g_{rr}} \left[ \left( g_{0\phi,\theta} - \frac{g_{0\phi}}{g_{00}} g_{00,\theta} \right) + \Omega \left( g_{\phi\phi,\theta} - \frac{g_{\phi\phi}}{g_{00}} g_{00,\theta} \right) \right. \right. \\ &+ \Omega^2 \left( \frac{g_{0\phi}}{g_{00}} g_{\phi\phi,\theta} - \frac{g_{\phi\phi}}{g_{00}} g_{0\phi,\theta} \right) \left. \right] \hat{r} \\ &+ \sqrt{g_{\theta\theta}} \left[ \left( g_{0\phi,r} - \frac{g_{0\phi}}{g_{00}} g_{00,r} \right) + \Omega \left( g_{\phi\phi,r} - \frac{g_{\phi\phi}}{g_{00}} g_{00,r} \right) \right. \\ &\left. + \Omega^2 \left( \frac{g_{0\phi}}{g_{00}} g_{\phi\phi,r} - \frac{g_{\phi\phi}}{g_{00}} g_{0\phi,r} \right) \right] \hat{\theta} \right]. \end{aligned} \quad (14)$$

For  $\Omega = 0$ , Eq. (14) reduces to

$$\begin{aligned} \tilde{\Omega}_p|_{\Omega=0} &= \frac{1}{2\sqrt{-g}} \left[ -\sqrt{g_{rr}} \left( g_{0\phi,\theta} - \frac{g_{0\phi}}{g_{00}} g_{00,\theta} \right) \hat{r} \right. \\ &\left. + \sqrt{g_{\theta\theta}} \left( g_{0\phi,r} - \frac{g_{0\phi}}{g_{00}} g_{00,r} \right) \hat{\theta} \right], \end{aligned} \quad (15)$$

which is only applicable outside the ergoregion. This is the LT precession frequency of a test gyro due to the rotation of any stationary and axisymmetric spacetime [12,13].

### A. Application to Kerr spacetime

We now apply the above formalism to the Kerr spacetime to describe the behavior of a test gyro both inside and outside the ergoregion. The Kerr metric in Boyer-Lindquist coordinates can be written as

$$\begin{aligned} ds^2 &= -\left( 1 - \frac{2Mr}{\rho^2} \right) dt^2 - \frac{4Mar \sin^2 \theta}{\rho^2} d\phi dt + \frac{\rho^2}{\Delta} dr^2 \\ &+ \rho^2 d\theta^2 + \left( r^2 + a^2 + \frac{2Mr a^2 \sin^2 \theta}{\rho^2} \right) \sin^2 \theta d\phi^2 \end{aligned} \quad (16)$$

where  $a$  is the specific angular momentum, defined as  $a = J/M$ , and

$$\rho^2 = r^2 + a^2 \cos^2 \theta, \quad \Delta = r^2 - 2Mr + a^2. \quad (17)$$

For convenience, we also define the dimensionless Kerr parameter  $a_* = a/M = J/M^2$ , which we shall use almost exclusively. The various metric components can be read off from Eq. (16) and we have

$$\sqrt{-g} = \rho^2 \sin \theta. \quad (18)$$

Substituting the metric components of Kerr spacetime into Eq. (14), we obtain the spin precession frequency of a gyroscope to be

$$\vec{\Omega}_p = \frac{A\sqrt{\Delta} \cos \theta \hat{r} + B \sin \theta \hat{\theta}}{\rho^3[(\rho^2 - 2Mr) + 4\Omega M a r \sin^2 \theta - \Omega^2 \sin^2 \theta (\rho^2 (r^2 + a^2) + 2Ma^2 r \sin^2 \theta)]}, \quad (19)$$

where

$$\begin{aligned} A &= 2aMr - \frac{\Omega}{8} [8r^4 + 8a^2r^2 + 16a^2Mr + 3a^4 + 4a^2(2\Delta - a^2) \cos 2\theta + a^4 \cos 4\theta] + 2\Omega^2 a^3 M r \sin^4 \theta, \\ B &= aM(r^2 - a^2 \cos^2 \theta) + \Omega [a^4 r \cos^4 \theta + r^2(r^3 - 3Mr^2 - a^2M(1 + \sin^2 \theta)) + a^2 \cos^2 \theta (2r^3 - Mr^2 + a^2M(1 + \sin^2 \theta))] \\ &\quad + \Omega^2 a M \sin^2 \theta [r^2(3r^2 + a^2) + a^2 \cos^2 \theta (r^2 - a^2)]. \end{aligned} \quad (20)$$

### B. Range of $\Omega$

Equation (19) is valid both inside and outside the ergoregion. From the requirement that  $u$  be timelike,

$$K^2 = g_{\phi\phi} \Omega^2 + 2g_{t\phi} \Omega + g_{tt} < 0, \quad (21)$$

we can calculate the restricted range of  $\Omega$ . Therefore, the allowed values of  $\Omega$  at any fixed  $(r, \theta)$  are

$$\Omega_-(r, \theta) < \Omega(r, \theta) < \Omega_+(r, \theta), \quad (22)$$

with

$$\Omega_{\pm} = \frac{-g_{t\phi} \pm \sqrt{g_{t\phi}^2 - g_{\phi\phi} g_{tt}}}{g_{\phi\phi}}. \quad (23)$$

Specifically, in the Kerr spacetime,

$$\Omega_{\pm} = \frac{2Mar \sin \theta \pm \rho^2 \sqrt{\Delta}}{\sin \theta [\rho^2 (r^2 + a^2) + 2Ma^2 r \sin^2 \theta]}, \quad (24)$$

which shows that the range of allowed values for  $\Omega$  becomes increasingly limited as the observer is located close to the horizon, that is,  $r \sim r_+$ , and is eventually limited to the single value at the horizon of the BH,

$$\Omega_H = \frac{a}{2Mr_+}. \quad (25)$$

Further, in the equatorial plane ( $\theta = \pi/2$ ), Eq. (24) becomes

$$\Omega_{\pm}|_{\theta=\pi/2} = \frac{2Ma \pm r\sqrt{\Delta}}{r(r^2 + a^2) + 2Ma^2}. \quad (26)$$

Since the ergoregion for NSs always extends all the way up to the ring singularity in the equatorial plane, we can

evaluate  $\Omega_{\pm}|_{\theta=\pi/2}$  at  $r = 0$  and, from Eq. (26), it is evident that these two frequencies match at the singularity. Therefore, we must point out that both at the horizon ( $r_+$ ) and at the ring singularity ( $r = 0, \theta = \pi/2$ ), there exist no valid values for  $\Omega$  (because of the strict inequality) implying that no timelike stationary observer can exist at these points. Our precession frequency expression is not valid at these points but it is still meaningful and illuminating to study and plot its limiting values at these points.

We can see from Fig. 1(a) that  $\Omega_+|_{\theta=\pi/2}$  and  $\Omega_-|_{\theta=\pi/2}$  match at  $r \rightarrow r_+$ , for a BH with  $a_* = 0.9$ , and the value of  $\Omega$  becomes  $\Omega_H \approx 0.31$ . Figure 1(c) shows that a small gap appears between the same two quantities at  $r \approx M$  in the case of the near-extremal NS with  $a_* = 1.001$  and the two curves match at  $r \rightarrow 0$  with the value of  $\Omega = 1/a_*$ . In the case of a NS with higher angular momentum, say, for  $a_* = 2$  [see Fig. 1(b)], the small gap disappears at  $r = M$  and the two curves match at  $r \rightarrow 0$ , as usual for NSs.

To compare the behavior of the gyro inside the ergoregion of a BH and NS, one can now plot  $\Omega_p = |\vec{\Omega}_p|$  with  $r$  at different  $\theta$  for observers with varying  $\Omega$ . For this purpose, we introduce the parameter  $q$  to scan the range of allowed values for  $\Omega$  as follows:

$$\begin{aligned} \Omega &= q\Omega_+ + (1 - q)\Omega_- \\ &= \omega - (1 - 2q) \sqrt{\omega^2 - \frac{g_{tt}}{g_{\phi\phi}}} \\ &= \frac{2Mar \sin \theta - (1 - 2q)\rho^2 \sqrt{\Delta}}{\sin \theta [\rho^2 (r^2 + a^2) + 2Ma^2 r \sin^2 \theta]}, \end{aligned} \quad (27)$$

where  $0 < q < 1$  and  $\omega = -g_{t\phi}/g_{\phi\phi}$ . Clearly, the range of  $q$  covers the entire range of  $\Omega$  from  $\Omega_+$  to  $\Omega_-$ . Now, using the expression for  $\Omega$ , from Eq. (27), we can simplify the denominator of Eq. (19) and obtain a nice and compact expression for the spin precession frequency,

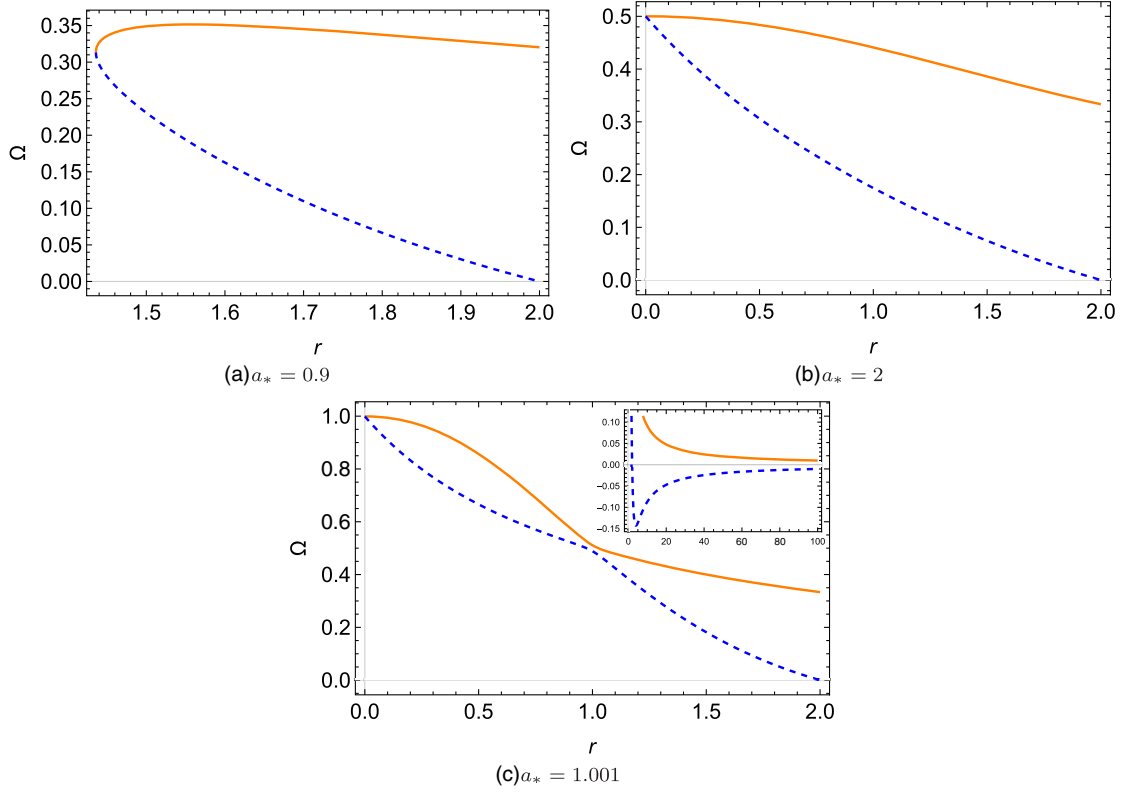


FIG. 1. The frequency of a stationary gyroscope  $\Omega$  can only take values in the range  $(\Omega_-, \Omega_+)$  at any  $(r, \theta)$ .  $\Omega_-$  and  $\Omega_+$  (in  $M^{-1}$ ) are shown as dashed blue and orange curves, respectively, and have been plotted specifically inside the ergoregion, in the equatorial plane ( $\theta = \pi/2$ ), as a function of  $r$  (in  $M$ ) for different values of Kerr parameter  $a_*$ . The inset in panel (c) shows  $\Omega_{\pm}$  outside the ergoregion, for reference. This is the boundary of the region in which the most general Killing vector in Kerr spacetime,  $K = \partial_0 + \Omega\partial_\phi$ , is timelike. For black holes, we can see from panel (a) that  $\Omega_{\pm}$  meet at the horizon. For NSs, we can see from panels (b) and (c) that  $\Omega_{\pm}$  meet at the singularity. Further, it can be seen from (c), that for near-extremal NSs ( $a_* \sim 1$ ),  $\Omega_{\pm}$  take close values near  $r = 1$ , which was the location of the horizon of the extremal BH ( $a_* = 1$ ).

$$\vec{\Omega}_p = \frac{(r^2 + a^2)^2 - a^2 \Delta \sin^2 \theta}{4q(1-q)\rho^7 \Delta} [A\sqrt{\Delta} \cos \theta \hat{r} + B \sin \theta \hat{\theta}], \quad (28)$$

where  $0 < q < 1$  and  $A$  and  $B$  have been given in Eq. (20).

If we use the expression for  $\Omega$  from Eq. (27) in Eq. (6), we obtain

$$K = \frac{qK_+ + (1-q)K_-}{\|qK_+ + (1-q)K_-\|} = \frac{qK_+ + (1-q)K_-}{\sqrt{2q(1-q)K_+ \cdot K_-}}, \quad (29)$$

where  $K_{\pm}$ , the two null vectors associated with  $\Omega_{\pm}$ , are given as [see Eq. (6)]

$$K_{\pm} = \partial_t + \Omega_{\pm} \partial_\phi. \quad (30)$$

Further, in a general stationary and axisymmetric spacetime, we can write  $K_+ \cdot K_- = 2(g_{tt} - \omega^2 g_{\phi\phi})$ .

### C. Acceleration of the test gyroscope

The gyroscopes we consider here have a specific velocity  $u$  and, in general, experience nonzero acceleration. They follow helical paths tangent to the Killing trajectory and the acceleration experienced by these gyroscopes is not arbitrary. This acceleration might be provided by using large amounts of rocket power or some other source of thrust, and we can calculate the necessary acceleration scalar, for our gyros, using the following expression of the four-acceleration:

$$\alpha_\beta = \frac{1}{2} \nabla_\beta \ln |K^2|. \quad (31)$$

We find the acceleration scalar for  $u$  to be

$$\begin{aligned} \alpha &= \sqrt{g^{\beta\gamma} \alpha_\beta \alpha_\gamma} \\ &= -\frac{1}{\rho^5 K^2} [\Delta \{M(2r^2 - \rho^2)[1 - a\Omega \sin^2 \theta]^2 - r\rho^4 \Omega^2 \sin^2 \theta\}^2 \\ &\quad + \sin^2 \theta \cos^2 \theta \{2Mr[a - \Omega(r^2 + a^2)]^2 + \Omega^2 \rho^4 \Delta\}^2]^{\frac{1}{2}}, \end{aligned} \quad (32)$$

where  $K^2$  is

$$K^2 = g_{\phi\phi}\Omega^2 + 2g_{t\phi}\Omega + g_{tt} \\ = \frac{-4q(1-q)\rho^2\Delta}{(r^2+a^2)^2 - a^2\Delta\sin^2\theta}. \quad (33)$$

Therefore, Eq. (32) reduces to

$$\alpha = \frac{(r^2+a^2)^2 - a^2\Delta\sin^2\theta}{4q(1-q)\rho^7\Delta} \\ \times [\Delta\{M(2r^2-\rho^2)[1-a\Omega\sin^2\theta]^2 - r\rho^4\Omega^2\sin^2\theta\}^2 \\ + \sin^2\theta\cos^2\theta\{2Mr[a-\Omega(r^2+a^2)]^2 + \Omega^2\rho^4\Delta\}^2]^{\frac{1}{2}}. \quad (34)$$

Equation (34) represents the amount of acceleration that is needed to move the test gyro in the Kerr spacetime. It is also evident from the above expression that the acceleration becomes arbitrarily high, blowing up as the event horizon is approached from any direction. Since NSs do not possess horizons, the acceleration of the gyro remains finite all along, including at  $r=0$  ( $\theta \neq \pi/2$ ), which we can see from

$$\alpha|_{r=0} = \frac{1}{4q(1-q)a^2\cos^3\theta} [M^2(1-a\Omega\sin^2\theta)^4 \\ + a^6\Omega^4\sin^2\theta\cos^2\theta]^{\frac{1}{2}}. \quad (35)$$

However, the above expression diverges close to the ring singularity ( $r=0, \theta = \pi/2$ ). The acceleration of the gyro [Eq. (32)] vanishes if it rotates in a geodesic with the Kepler frequency

$$\Omega = \Omega_\phi = \pm \frac{M^{\frac{1}{2}}}{r^{\frac{3}{2}} \pm aM^{\frac{1}{2}}}. \quad (36)$$

where we have used, from Eq. (20),

$$A|_{r=0} = -\frac{a^4\Omega}{8}[3+4\cos 2\theta + \cos 4\theta], \\ B|_{r=0} = -Ma^3\cos^2\theta[1-a\Omega(1+\sin^2\theta) + a^2\Omega^2\sin^2\theta]. \quad (39)$$

In the above expressions, the allowed range of  $\Omega$  is

$$-\frac{1}{a\sin\theta} < \Omega < \frac{1}{a\sin\theta}. \quad (40)$$

Since we are outside the ergoregion, we can consider static observers, that is, we set  $\Omega = 0$ , and so Eq. (38) reduces to

## D. Zero angular momentum observer

We note that for  $q = 0.5$ ,  $\Omega$  becomes the characteristic zero-angular-momentum-observer (ZAMO) frequency  $\omega$ ,

$$\omega = \frac{2Mar}{(r^2+a^2)^2 - a^2\Delta\sin^2\theta} = -\frac{g_{t\phi}}{g_{\phi\phi}}. \quad (37)$$

In this case, test gyros attached to stationary observers regard both  $+\phi$  and  $-\phi$  directions equivalently, in terms of the local geometry, and see photons symmetrically [9]. These gyros are nonrotating relative to the local spacetime geometry. The angular momentum of such a ‘‘locally nonrotating’’ observer is zero and is therefore called a ZAMO, first introduced by Bardeen [9,14]. Bardeen *et al.* [15] showed that the ZAMO frame is a powerful tool in the analysis of physical processes near astrophysical objects. Here, we should note that Eq. (31) reduces to Eq. (33.23) of [9] (see Exercise 33.4) in the case of a ZAMO in a general stationary and axisymmetric spacetime.

## IV. USEFUL LIMITS

In this section, we will explore various useful limits of the spin precession frequency [Eq. (28)]. We discuss what happens to the frequency as  $r \rightarrow 0$  (specifically, the ring singularity is at  $r=0, \theta = \pi/2$ ), what it looks like in the equatorial plane  $\theta = \pi/2$ , and whether this frequency vanishes in the Schwarzschild spacetime.

### A. Behavior of $\vec{\Omega}_p$ at $r=0$

As discussed earlier, our expression for  $\vec{\Omega}_p$  is not valid at the ring singularity ( $r=0, \theta = \pi/2$ ). However, we can still study its behavior in its vicinity, that is, in the region  $r=0, 0 \leq \theta < 90^\circ$ . We note here that this region is strictly completely outside the ergoregion since the ergosurface meets the ring singularity (see Figs. 1 and 2 of Ref. [3]). At  $r=0$ , Eq. (19) becomes

$$\vec{\Omega}_p|_{r=0} = \frac{-a^2\Omega[3+4\cos 2\theta + \cos 4\theta]\hat{r} - 4M\sin 2\theta[1-a\Omega(1+\sin^2\theta) + a^2\Omega^2\sin^2\theta]\hat{\theta}}{8a^2\cos^4\theta[1-a^2\Omega^2\sin^2\theta]}, \quad (38)$$

$$|\vec{\Omega}_p| = \frac{M}{a^2} \tan\theta \sec^2\theta, \quad (41)$$

matches with our earlier calculations of Ref. [3], and can be seen from Eqs. (6) and (7) therewith. Therefore,  $\Omega_p$  varies from  $0 \leq \Omega_p < \infty$  for  $0 \leq \theta < 90^\circ$  at  $r=0$ . That is, it diverges only on the ring singularity (which is at  $x^2+y^2=a^2, z=0$ , in Cartesian Kerr-Schild coordinates) but is finite *inside* it ( $x^2+y^2 < a^2, z=0$ ).

It is useful to mention here that one can smoothly, in principle, go over to the region with negative  $r$  (i.e.,  $r < 0$ ) in Kerr spacetime, which is tantamount to passing through

the ring singularity, but we stop at  $r = 0$  and avoid probing negative values of  $r$ . The reason behind stopping at  $r = 0$  is that it is fairly widely accepted that quantum gravity will resolve the singularity resulting in a compact overspinning object with a boundary at a positive value of  $r$ , which is referred to as a ‘‘superspinar’’ [16]. Thus the region with negative values of  $r$  will be excised and pathological features such as closed timelike curves which occur in the  $r < 0$  region will not arise. Thus we restrict our probe of the Kerr spacetime to  $r \geq 0$ .

### B. Behavior of $\vec{\Omega}_p$ in the equatorial plane, $\theta = \pi/2$

The precession frequency in the equatorial plane is

$$\vec{\Omega}_p|_{\theta=\pi/2} = \frac{aM + \Omega(r^3 - 3Mr^2 - 2Ma^2) + aM\Omega^2(3r^2 + a^2)}{r^2[(r-2M) + 4\Omega Ma - \Omega^2[r(r^2 + a^2) + 2Ma^2]]}, \quad (42)$$

with the range  $\Omega$  determined from Eq. (26). Specifically, at the ergosurface ( $r = 2M$ ) the precession frequency becomes

$$\vec{\Omega}_p|_{\theta=\pi/2, r=2M} = \frac{a - 2\Omega(a^2 + 2M^2) + a\Omega^2(a^2 + 12M^2)}{16\Omega M^2[a - \Omega(a^2 + 2M^2)]} \quad (43)$$

with  $\Omega$  being restricted to (see Fig. 1 also)

$$0 < \Omega < \frac{a}{a^2 + 2M^2}. \quad (44)$$

That is, if the mass or angular momentum of the central object increases, the allowed range of  $\Omega$  at the ergosurface, in the equatorial plane, decreases.

For extremal BHs ( $a_* = 1$ ), the precession frequencies at the outer ergoregion and at the outer event horizon, respectively, can be obtained as

$$\vec{\Omega}_p|_{\theta=\pi/2, r=2M, a_*=1} = \frac{1 - 6\Omega M + 13\Omega^2 M^2}{16\Omega M^2[1 - 3\Omega M]},$$

$$\vec{\Omega}_p|_{\theta=\pi/2, r=M, a_*=1} = -\frac{1}{M}. \quad (45)$$

### C. Nonzero $\vec{\Omega}_p$ in the Schwarzschild spacetime

Now, if we set  $a = 0$ , the Kerr spacetime reduces to the Schwarzschild spacetime, which is *nonrotating*. From Eq. (19), we obtain

$$\vec{\Omega}_p|_{a=0} = \Omega \frac{(r-3M) \sin \theta \hat{\theta} - (r^2 - 2Mr)^{\frac{1}{2}} \cos \theta \hat{r}}{r - 2M - r^3 \Omega^2 \sin^2 \theta}, \quad (46)$$

where  $\Omega$  can take any value such that  $u$  is timelike. Since the Schwarzschild spacetime is spherically symmetric, we can write Eq. (46) for  $\theta = \pi/2$  as

$$\Omega_p|_{a=0} = \Omega \frac{r - 3M}{r - 2M - r^3 \Omega^2}. \quad (47)$$

This means that a gyroscope moving in the Schwarzschild spacetime, which is a static spacetime, will precess. Now, if the gyro moves along a circular geodesic, then  $\Omega$  should be the Kepler frequency, i.e.,  $\Omega_{\text{Kep}} = (M/r^3)^{1/2}$ , and Eq. (47) reduces to

$$\Omega_p|_{a=0, \Omega=\Omega_{\text{Kep}}} = \Omega = \left(\frac{M}{r^3}\right)^{\frac{1}{2}}. \quad (48)$$

The above expression gives the precession frequency in the Copernican frame, computed with respect to the proper time  $\tau$ . The proper time  $\tau$ , measured in the Copernican frame, is related to the coordinate time  $t$  via  $d\tau = \sqrt{1 - \frac{3M}{r}} dt$  and we can obtain the precession frequency in the coordinate basis  $\Omega'$  as

$$\Omega' = \left(\frac{M}{r^3}\right)^{\frac{1}{2}} \sqrt{1 - \frac{3M}{r}}. \quad (49)$$

We can now find the frequency associated with the change in the angle of the spin vector over, say, one complete revolution around the central object. This is just the difference of  $\Omega'$  and  $\Omega$  [17], and we get

$$\Omega_{\text{geodetic}} = \left(\frac{M}{r^3}\right)^{\frac{1}{2}} \left(1 - \sqrt{1 - \frac{3M}{r}}\right), \quad (50)$$

where we have identified above that this precession is just due to geodetic precession ( $\Omega_{\text{geodetic}}$ ). This agrees with standard results [18].

## V. DISTINGUISHING KERR NAKED SINGULARITIES FROM KERR BLACK HOLES USING THE PRECESSION OF A TEST GYRO

In this section, we point out the characteristic differences in the behavior of the modulus of the spin precession frequency ( $\Omega_p$ ) of stationary gyroscopes for BHs and NSs. We show that the value of  $\Omega_p$  becomes arbitrarily large for such gyroscopes, located arbitrarily close to the horizon of a BH, that is,  $r \sim r_+$ , for all values of  $q$  except  $q = 0.5$ , the ZAMO frequency. However, for a NS,  $\Omega_p$  always remains finite up to  $r = 0$ , except for  $r = 0$  and  $\theta \sim \pi/2$ , i.e., near the singularity.

We obtain distinguishing characteristic features specifically in the radial profile of  $\Omega_p$  for both the BH and NS cases, which we will discuss as we proceed. Further, we also obtain features in the radial profile of  $\Omega_p$  that could help distinguish near-extremal NSs from those with higher spin. We explore the details of such features and provide a

criterion to separate near-extremal NSs ( $1 < a_* < 1.1$ ) from those with higher spins ( $a_* \geq 1.1$ ) in Sec. VI.

We plot the modulus of the precession frequency of stationary gyros  $\Omega_p = |\Omega_p|$ , obtained from Eq. (28),

$$\Omega_p = \frac{(r^2 + a^2)^2 - a^2 \Delta \sin^2 \theta}{4q(1-q)\rho^7 \Delta} \sqrt{A^2 \Delta \cos^2 \theta + B^2 \sin^2 \theta}, \quad (51)$$

and study its variation with  $a_*$ ,  $q$ ,  $r$ , and  $\theta$ . Briefly, from the above expression, one can see that the denominator of  $\Omega_p$  vanishes for  $\rho = 0$ ,  $\Delta = 0$ , or  $q = 0, 1$ . Since it can be seen from Eq. (20) that  $A$  and  $B$  are finite valued,  $\Omega_p$  becomes arbitrarily large when its denominator vanishes.  $\rho = 0$  is the ring singularity,  $\Delta = 0$  is the event horizon, and  $q = 0, 1$  are the (excluded) boundaries of the allowed values of  $\Omega$ .

For a BH with  $a_* = 0.9$ , we can see from the left panels of Fig. 2 that the precession frequency indeed becomes arbitrarily large close to the horizon for all values of  $a_*$ ,  $q$ , and  $\theta$ , except  $q = 0.5$ . From Fig. 2(a), we can see that for  $q < 0.5$  the radial variation of  $\Omega_p$  is monotonic, with no maxima or minima. However, for  $q > 0.5$ , a minimum starts appearing, which can be seen from Fig. 2(e), and this minimum is sharp for  $\theta = \pi/2$ . For observers at the ZAMO frequency,  $q = 0.5$ , the precession frequency remains smooth and finite, as can be seen from Fig. 2(c), even for gyros orbiting close to the horizon. We note that the ZAMO frequency exhibits consistently peculiar behavior, which might lead to interesting insights upon further exploration. On the other hand, for a NS with  $a_* = 1.1$ , as can be seen from the plots on the right in Fig. 2, the spin precession frequency does not diverge. It remains finite and regular even as one approaches  $r = 0$  for all angles  $0 < \theta \lesssim 90^\circ$ . Near  $r = 0$ ,  $\theta = 90^\circ$ , the precession frequency becomes arbitrarily large because of the presence of the ring singularity. This is also in stark contrast to the BH case in the present paper, for which we obtain a divergence in the precession frequency close to the event horizon, far away from  $r = 0$ . One also finds that a local minimum and a local maximum appear for  $q \geq 0.5$  for some angles; i.e., there are additional features that might help to ascertain the angular velocity of a stationary observer with respect to the ZAMO frequency. We also note here that it can be seen from the y-axis scales in Figs. 2(a), 2(b), 2(e), and 2(f) relative to the scales in the other panels that  $\Omega_p$  rises sharply as the angular momentum of the stationary observer  $\Omega$  nears its allowed bounding values  $\Omega_\pm$ . These panels represent  $q = 0.1, 0.9$ , respectively, for a BH and a NS.

In Fig. 3, we demonstrate that the features obtained for  $a_* = 0.9$  are characteristic of all BHs by plotting  $\Omega_p$  for other values of  $a_* = 0.2, 0.4, 0.6, 0.8, 1$ . We show that the spin precession frequency is finite and smooth both inside and outside the ergoregion, but it diverges near the horizon for all  $a_*$ ,  $q$ ,  $r$ , and  $\theta$ , except for  $q = 0.5$ . Finally, in Fig. 4,

we demonstrate that the features obtained for  $a_* = 1.1$  are characteristic of NSs, in general, by considering other values of  $a_* = 1.01, 1.05, 1.09, 2, 5$ . We have picked these values at nonuniform intervals, anticipating additional features in the plots for near-extremal NSs. We show that the spin precession frequency is finite and smooth both inside and outside of the ergoregion, the same as in the BH case, but it diverges near the ring singularity for all  $a_*$ ,  $q$ ,  $r$ , and  $\theta$ . This is different from the BH case, as we have already mentioned above. Indeed, we also note here that near-extremal NSs appear to have additional characteristic features which could be used to distinguish them from other generic higher spin NSs, as can be seen clearly from the panels of this figure, and we explore this observation in the following section.

We now describe our experiment to distinguish a Kerr black hole from a Kerr naked singularity. Consider gyroscopes attached to stationary observers with a nonzero azimuthal component ( $\Omega$ ) to their four-velocities  $u$ . These are observers moving along circles at constant  $r$  and  $\theta$ , with a constant angular velocity  $\Omega$ . For every orbit or trajectory at fixed  $(r, \theta)$ , we can find the range of allowed  $\Omega(r, \theta)$  by finding the lower and upper bounds,  $\Omega_-(r, \theta)$  and  $\Omega_+(r, \theta)$ . We can represent this angular velocity equivalently by the parameter  $q$ , which gives the absolute relation of that observer with respect to the ZAMO ( $q = 0.5$ ). Consider observers along two directions, say  $\theta = \theta_1, \theta_2$  ( $\theta_1 \sim \theta_2$ ). From the modulus of the precession frequencies  $\Omega_p$  of gyroscopes attached to timelike stationary observers orbiting a Kerr compact object at different  $r$  along these two directions, we can make the following statements: (i) if  $\Omega_p$  becomes arbitrarily large in the limit of approach to the central object for both  $\theta_1$  and  $\theta_2$ , then the spacetime contains a black hole, whereas (ii) if  $\Omega_p$  becomes arbitrarily large in the limit of approach to the central object for at most one of the two directions  $\theta_1, \theta_2$ , then the spacetime contains a naked singularity. The reason for this distinction is as follows. For a black hole,  $\Omega_p$  becomes arbitrarily large in the limit of approach to the event horizon, which exists in all directions (i.e., for all  $\theta$ ) and therefore, observers approaching the black hole in all directions will display a divergence. However, for a naked singularity, since the divergence occurs only close to the ring singularity, which exists in the equatorial plane ( $\theta = \pi/2$ ), only those observers that approach the compact object approximately along this direction will see a divergence. Therefore, if one of  $\theta_1, \theta_2 = \pi/2$ , then we will see a divergence only along that direction. Or, if neither  $\theta_1, \theta_2 \neq \pi/2$ , we will not see any divergence. Therefore, a divergence along at most one direction will indicate that the spacetime contains a naked singularity. We also note here that our statements are qualitatively independent of the mass of the compact object.

Finally, we expect that these results can possibly be extended to any black hole or naked singularity with

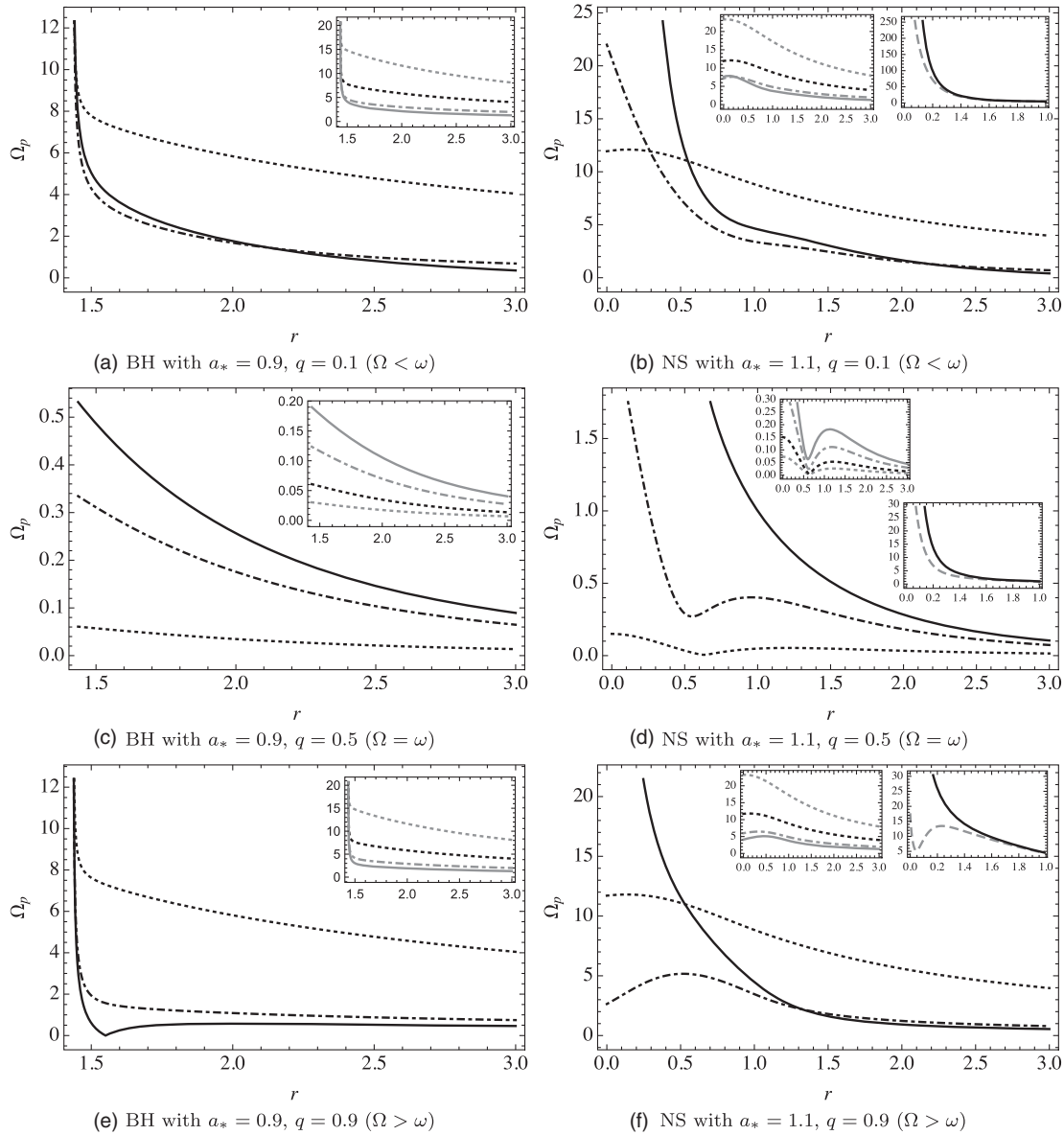


FIG. 2. We have plotted in each panel the modulus of the precession frequency of stationary gyroscopes  $\Omega_p$  (in  $M^{-1}$ ) versus  $r$  (in  $M$ ) around a black hole (left panels) with  $a_* = 0.9$  and a naked singularity (right panels) with  $a_* = 1.1$  for different  $q$  and  $\theta$ . Each of the rows has a different value of  $q$ , which measures its angular velocity, and in each panel,  $\theta$  takes values  $10^\circ$ ,  $50^\circ$ ,  $90^\circ$  represented in dotted black, dotted-dashed black, and solid black curves, respectively. For the BH,  $r$  ranges from the horizon radius (which is at  $\sim 1.44$ , in this case) to 3. For the NS, the plots begin from  $r = 0$  (specifically, the singularity is at  $r = 0$  and  $\theta = 90^\circ$ ) and go to 3, and the ergosurface is at 2 for  $\theta = 90^\circ$ . It can be seen that there is a much bigger drop in  $\Omega_p$  from  $10^\circ$  to  $50^\circ$  than from  $50^\circ$  to  $90^\circ$ . We have therefore given inset plots (left inset for NS panels) for additional  $\theta$  values (close to the pole) of  $5^\circ$ ,  $20^\circ$ , and  $30^\circ$  in dotted gray, dotted-dashed gray, and solid gray curves, along with  $10^\circ$  in a dotted black curve, the same as in the main panel. Further, for the NS case, since the singularity is at  $\theta = 90^\circ$  in these coordinates, as  $r \rightarrow 0$ ,  $\theta \rightarrow 90^\circ$ , the frequency blows up. We have zoomed in on the range of  $r$  between 0 and 1 and set insets (on the right in the NS panels) of the plots for  $\theta = 80^\circ$ ,  $90^\circ$  in dashed gray and solid black curves to demonstrate how quickly  $\Omega_p$  increases relative to angles much smaller than  $90^\circ$ .

symmetries. We have used in [3] and in this work the result that there exist invariant characterizations of ergoregions (for rotating spacetimes) and horizons, respectively, in terms of the Killing vectors. We set up observers equipped with gyroscopes along integral curves of these Killing

vectors. We then study the precession behavior of these gyros and interpret any arbitrarily large growth in the modulus of the precession frequency that is obtained as indicators of the presence of an ergosurface, as in [3], or a horizon, as we have discussed here.

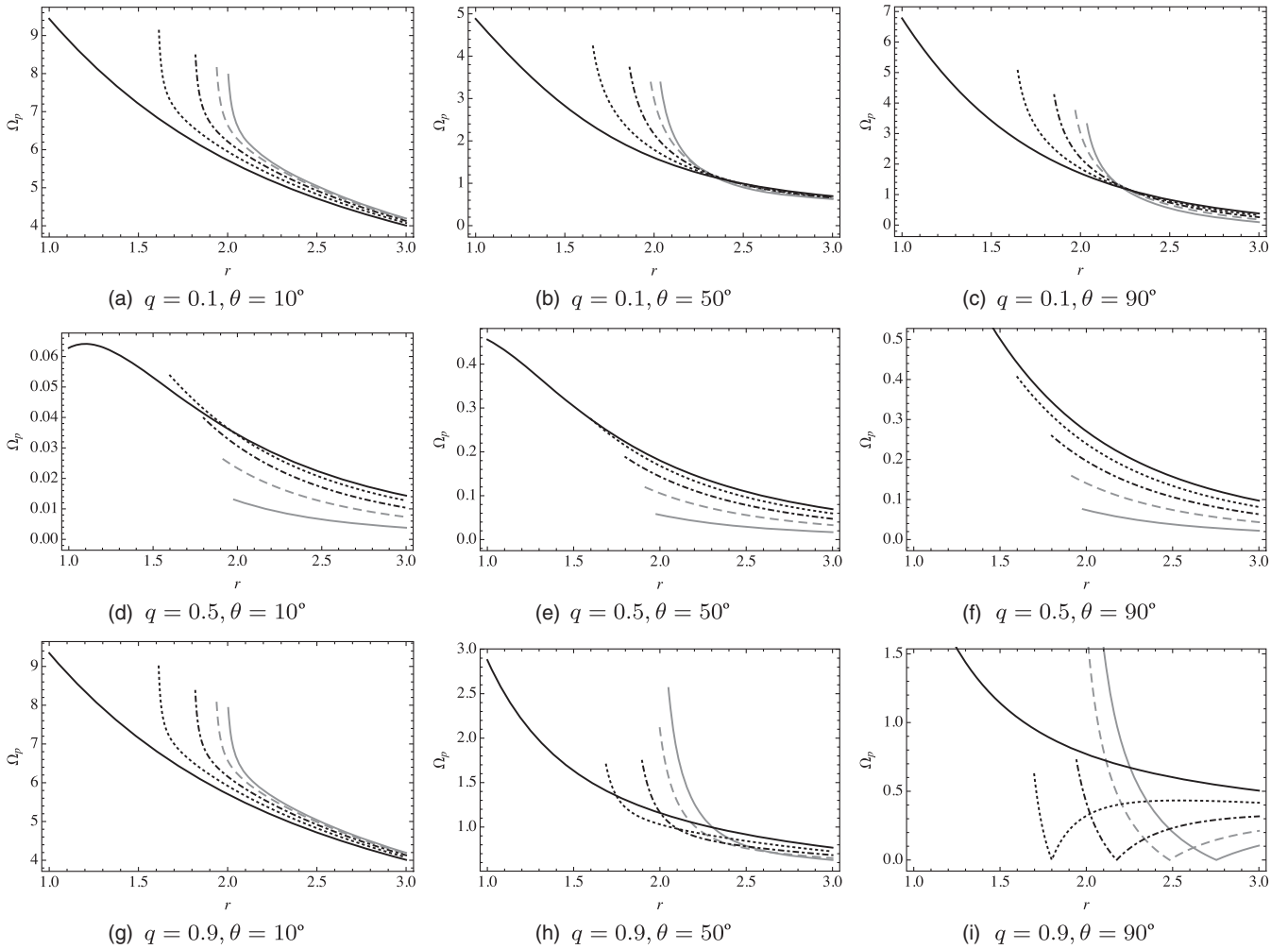


FIG. 3. We have plotted here, for black holes, the modulus of the precession frequency  $\Omega_p$  (in  $M^{-1}$ ) versus  $r$  (in  $M$ ) for different  $a_*$ ,  $q$ , and  $\theta$ . We have  $q = 0.1, 0.5, 0.9$  in the top, middle, and bottom rows, respectively, and  $\theta = 10^\circ, 50^\circ, 90^\circ$  in the left, center, and right columns, respectively. In each panel, solid gray, dashed gray, dotted-dashed black, dotted black, and solid black curves stand for  $a_* = 0.2, 0.4, 0.6, 0.8, 1$ , respectively. We have plotted  $\Omega_p$  for each BH (with different  $a_*$ ) between its horizon radius ( $r_+$ ) and  $r = 3$ . The ergoregion is at  $r = 2$  for  $\theta = 90^\circ$  (bottom row), for reference. This figure clearly demonstrates that for all values of  $a_*$ ,  $q$ ,  $\theta$ , the precession frequency  $\Omega_p$  becomes arbitrarily large near the event horizon, in general. As can be seen from the bottom row, for  $q > 0.5$ , minimas appear. Specifically, from panel (i), it can be seen that the sharpness of the minimas increases with  $a_*$ , with extremal black holes as exceptions.

## VI. DISTINGUISHING NEAR-EXTREMAL KERR NAKED SINGULARITIES FROM ONES WITH HIGHER ANGULAR MOMENTUM

In the previous section, we discussed how the spin precession frequency, in the case of a BH, becomes arbitrarily large at the horizon for all values of  $q$ , barring  $q \sim 0.5$ . For a NS, it diverges only near the ring singularity  $r = 0$ ,  $\theta = \pi/2$  and remains finite even for  $r = 0$  for  $0 < \theta \lesssim \pi/2$ . We pointed out that this can be used to distinguish a BH from a NS. Further, from Fig. 4, a general feature that emerges is that with increasing  $a_*$ , the radial profile of  $\Omega_p$  becomes increasingly “smoother.” This motivates us to use the “sharp” features that appear for naked singularities, with  $a_* \gtrsim 1$  to separate them from

those with  $a_* \gg 1$ . Indeed, we find that one can use the features that appear for  $1 < a_* < 1.1$  to characterize them and potentially distinguish them from  $a_* > 1$ . In this section we highlight these features in  $\Omega_p(r)$  with changes in  $a_*$ ,  $q$ ,  $\theta$ .

We place emphasis on this study because of the importance of near-extremal naked singularities in general relativity. For example, in a black hole binary collision, like the one studied by LIGO recently, the angular momentum of the compact object during the collision could temporarily exceed the Kerr bound and result in a temporary near-extremal naked singularity, a scenario that is of interest to the authors of [19]. Further, if a thick accretion disk could spin up a near-extremal black hole, it would likely form a

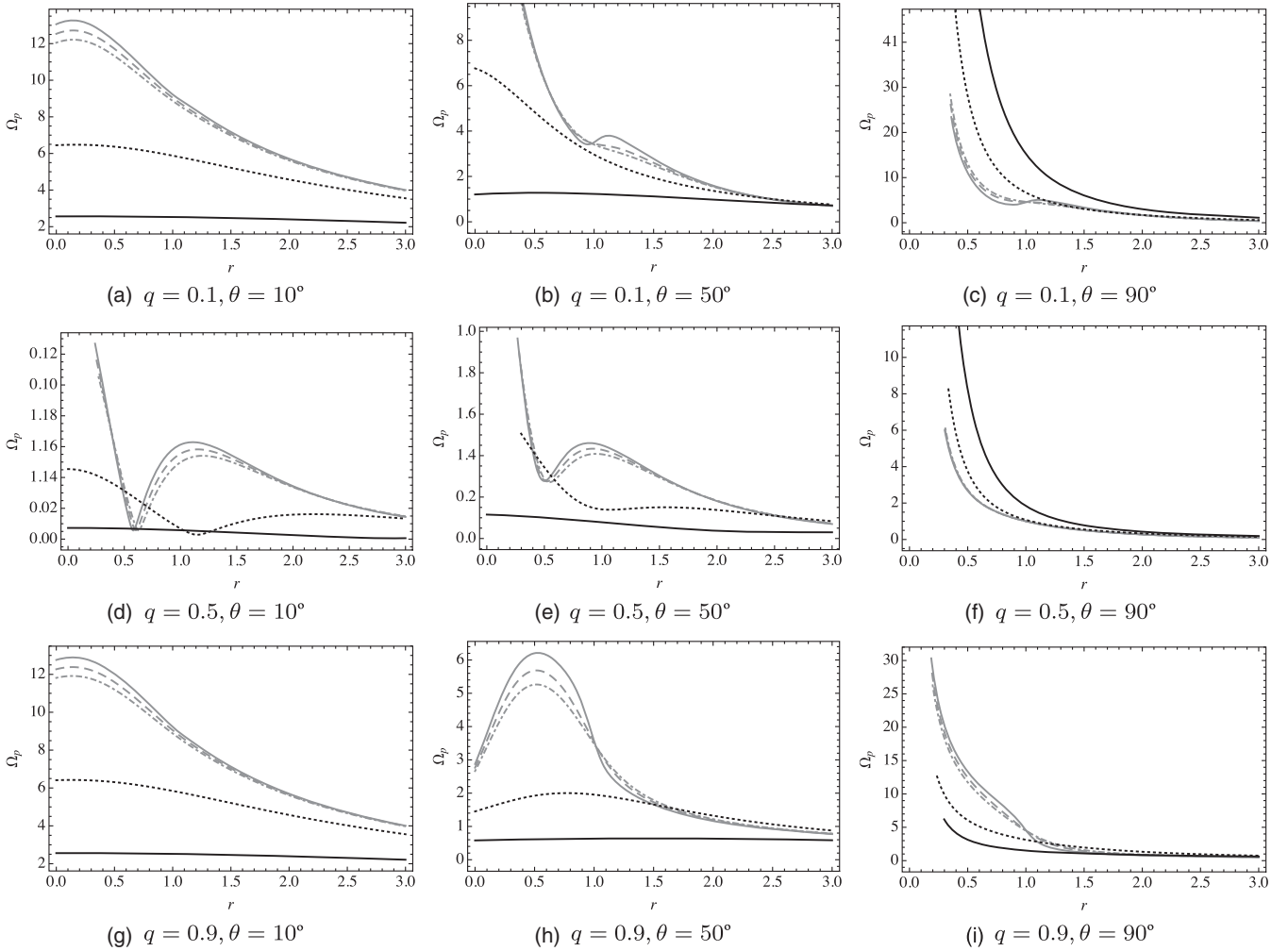


FIG. 4. We have plotted here, for naked singularities, the modulus of the precession frequency  $\Omega_p$  (in  $M^{-1}$ ) versus  $r$  (in  $M$ ) for different  $a_*$ ,  $q$ , and  $\theta$ . We have  $q = 0.1, 0.5, 0.9$  in the top, middle, and bottom rows, respectively, and  $\theta = 10^\circ, 50^\circ, 90^\circ$  in the left, center, and right columns, respectively. In each panel, solid gray, dashed gray, dotted-dashed gray, dotted black, and solid black curves stand for  $a_* = 1.01, 1.05, 1.09, 2, 5$ , respectively. We have plotted  $\Omega_p$  for each NS (with different  $a_*$ ) between  $r = 0$  and  $r = 3$ . The ergoregion is at  $r = 2$  for  $\theta = 90^\circ$  (bottom row), for reference. This figure clearly demonstrates that for all values of  $a_*$ ,  $q$ ,  $\theta$ , the precession frequency  $\Omega_p$  becomes arbitrarily large near the ring singularity. Further, the gray curves are all near-extremal NSs and this figure demonstrates how near-extremal NSs appear to have additional characteristic features that can be used to distinguish them from NSs with higher angular momentum. Motivated thus, we explore this distinction in greater detail in Sec. VI, since near-extremal naked singularities are of great interest from an observational standpoint, if they exist.

near-extremal naked singularity due to its proximity to the black hole geometry in the  $a_*$  parameter space. We mention in relation to this point that using the Polish doughnut model (not for Kerr spacetime), Li and Bambi [20] showed that the overspinning compact objects can be generated by thick accretion disks.

The radial variation of the modulus of the precession frequency for all  $q$ , at  $\theta \sim 0^\circ$ , is smooth, as can be seen from Figs. 5 and 6. For an observer moving with an angular velocity that is not close to the ZAMO frequency ( $q \sim 0.5$ ), a clear maximum-minimum pair appears around  $r = 1$ , resulting in a sharp drop/rise in  $\Omega_p$  at that radius, as can be seen from Figs. 5(a) and 5(e). The event horizon of an

extremal black hole  $a_* = 1$  is located at  $r = 1$  and we link this sharp feature to this observation. We will discuss this in some more detail in the following subsection. Roughly, however, the reason for these sharp features is as follows. From Eq. (51), we see that  $\Delta$  appears in the denominator. We know that  $\Delta = 0$  marks the location of the horizon for  $a_* \leq 1$  and specifically, because of this, for  $a_* = 1$ ,  $\Omega_p$  exhibits a divergence at  $r = 1$ . This divergence is avoided for  $a_* \gtrsim 1$  since  $\Delta \neq 0$ , but  $\Delta$  changes only slightly from 0 and hence we see a sharp change at  $r \sim 1$ . The dependence on  $\theta$  is due to the other factors in Eq. (51). That is,  $a_* \gtrsim 1$  naked singularities feel the “phantom effects” of the extremal event horizon. Further, we can ascertain whether

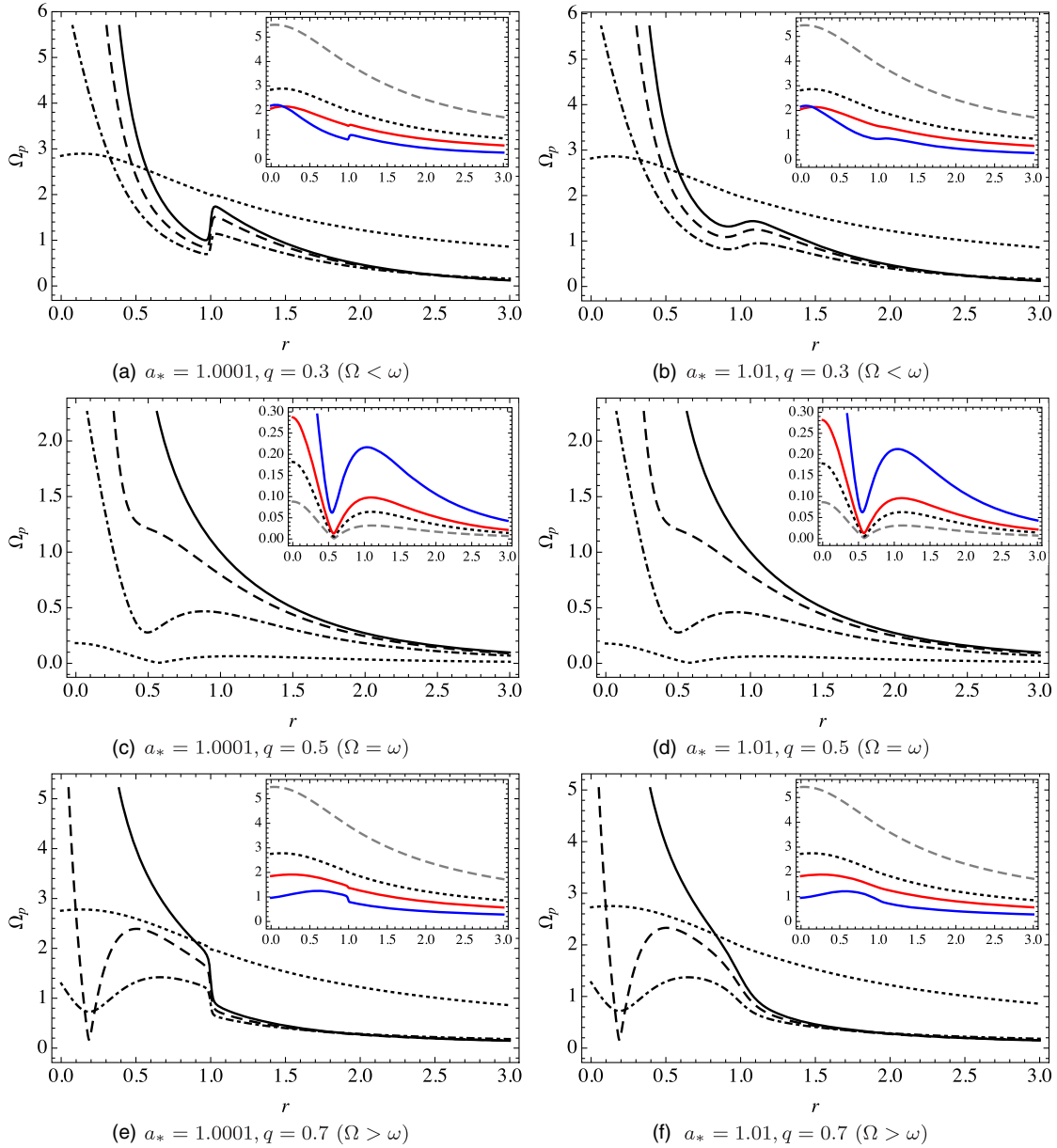


FIG. 5. The modulus of the precession frequency  $\Omega_p$  (in  $M^{-1}$ ) versus  $r$  (in  $M$ ) has been plotted for near-extremal naked singularities with two different  $a_*$  for different  $q, \theta$ . We have used  $a_* = 1.0001, 1.01$  in the plots in the left and right columns and  $q = 0.3, 0.5, 0.7$  in the top, middle, and bottom rows, which are representative of  $\Omega < \omega$ ,  $\Omega = \omega$ , and  $\Omega > \omega$ , respectively. In each panel, the dotted black, dotted-dashed black, dashed black, and solid black curves represent  $\theta = 10^\circ, 50^\circ, 70^\circ, 90^\circ$ , respectively. This plot shows that for all  $q$ , at  $\theta \sim 0^\circ$ , the radial variation of  $\Omega_p$  is smooth. From panels (a), (e), for  $\Omega \approx \omega$ , a clear maximum-minimum pair appears around  $r = 1$ , resulting in a sharp drop/rise in  $\Omega_p$  at that radius. The event horizon of an extremal black hole  $a_* = 1$  is located at  $r = 1$ , and we link this sharp feature to this observation. At  $\Omega = \omega$  itself,  $\Omega_p$  is smooth, devoid of this particular feature. We discuss  $\Omega \sim \omega$  in the next figure since these  $q$  values have richer features. As can be seen from panels (b), (f), this sharp rise/drop in  $\Omega_p$  gets smoother with increasing  $a_*$ . By  $a_* \sim 1.1$ , these features completely vanish and we interpret this feature as providing an important criterion based on which one can distinguish a near-extremal NS ( $1 < a_* < 1.1$ ) from a NS with a higher spin. In the inset, we display approximately at what angle  $\theta$  this sharp  $r = 1$  feature starts to appear from, and we have used  $\theta = 5^\circ, 10^\circ, 15^\circ, 30^\circ$  for the dashed gray, dotted black (same as the main panel), red, and blue curves, respectively.

an observer is rotating with an angular frequency  $\Omega$  above or below the ZAMO frequency  $\omega$ ; that is, we can distinguish whether  $\Omega > \omega$  or  $\Omega < \omega$ , by looking at the additional maxima-minima structure in the region  $r < 1$ .

We note here that at  $\Omega = \omega$  itself  $\Omega_p$  is smooth, as can be seen from Figs. 5(c) and 5(d), and it is devoid of the sharp features that are obtained at  $r = 1$  for  $q \approx 0.5$ . Features for  $q \sim 0.5$  are highlighted in Fig. 6.

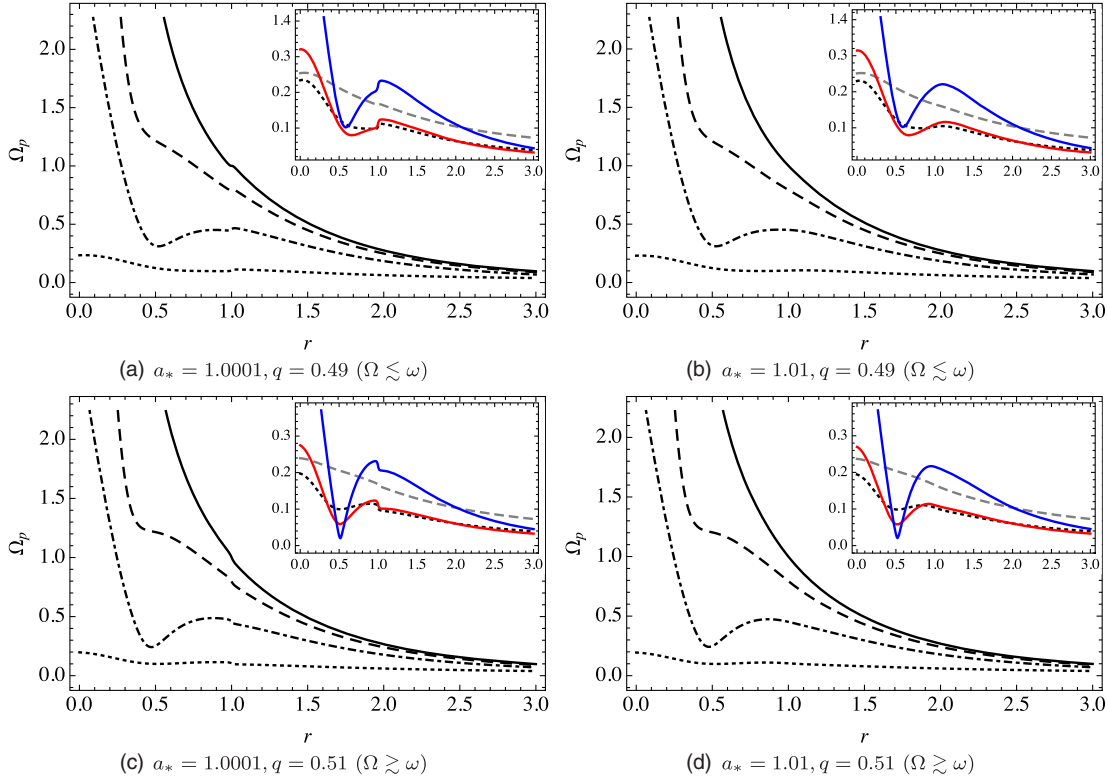


FIG. 6. We plot now  $\Omega_p$  (in  $M^{-1}$ ) versus  $r$  (in  $M$ ) for near-extremal naked singularities with  $a_* = 1.0001$  and  $1.01$  at different  $\theta$ , for  $q \sim 0.5$  ( $q \neq 0.5$ ). The curve styles are the same as in Fig. 5 and the insets in this figure demonstrate that for these values of  $q$ , that is,  $q$  close to but not equal to  $0.5$ , there are richer features at smaller angles  $\theta$ . It can be seen from this figure, as from Fig. 5, that with increasing  $a_*$ , these features all get smoothed out.

On moving closer to the compact object, that is, on decreasing  $r$ , in any direction  $\theta$ ,  $\Omega_p$  always increases. Further, for  $r \rightarrow 0$ , on increasing  $\theta$ , observers get closer to the ring singularity and therefore see a rapidly rising  $\Omega_p$ . Specifically, as  $\theta \rightarrow \pi/2$ ,  $\Omega_p$  becomes unbounded. With an increase in  $a_*$ , as is demonstrated in both Figs. 5 and 6, we see that this  $r = 1$  feature becomes smoother. By  $a_* \sim 1.1$ , these features completely vanish and we interpret this result as providing an important criterion based on which one can distinguish a near-extremal NS ( $1 < a_* < 1.1$ ) from one with a higher spin. In the insets of both figures, we explore approximately at what angle  $\theta$  this sharp  $r = 1$  feature starts to appear from and this value of  $\theta$  depends on  $a_*$ , in general.

### A. Behavior of gyro frequency for near-extremal naked singularities

In this subsection, we will discuss the reasons for the features that are exhibited by near-extremal naked singularities that are different from those with higher spins. We define  $\chi$  from Eq. (28) for convenience as

$$\chi = \frac{(r^2 + a^2)^2 - a^2 \Delta \sin^2 \theta}{4q(1-q)\rho^7 \Delta}, \quad (52)$$

so that the precession frequency  $\vec{\Omega}_p$  becomes

$$\vec{\Omega}_p = \chi [A \sqrt{\Delta} \cos \theta \hat{r} + B \sin \theta \hat{\theta}]. \quad (53)$$

First, we dedimensionalize the above expression by replacing  $a_* = a/M$  and introducing the dimensionless radial variable  $y = r/M$ . We can then write  $\chi$  as

$$\chi = \frac{(y^2 + a_*^2)^2 - a_*^2 \Delta_* \sin^2 \theta}{4q(1-q)\rho_*^7 \Delta_*} M^{-5}. \quad (54)$$

Therefore,  $\chi$  has mass dimension  $-5$ . Similarly,  $A$  and  $B$  have mass dimensions 3 and 4, respectively,  $\sqrt{\Delta}$  has mass dimension 1 and the term in the square braces of Eq. (53) has a total mass dimension of 4. Therefore,  $\vec{\Omega}_p$  has an overall mass dimension of  $-1$ . In this section, henceforth, we work exclusively with dimensionless quantities and simply drop all factors of  $M$ . We write down now the dimensionless expressions for a near-extremal NS by replacing  $a_* = 1 + \epsilon$  ( $\epsilon > 0$ ),

$$\begin{aligned}
\chi_{\text{ne}} &= \frac{(y^2 + 1 + 2\epsilon)^2 - (1 + 2\epsilon)\Delta_{\text{ne}}\sin^2\theta}{4q(1-q)\rho_{\text{ne}}^7\Delta_{\text{ne}}}, \\
A_{\text{ne}} &= 2(1+\epsilon)y - \frac{\Omega_{\text{ne}}}{8}\{8y^4 + 8(1+2\epsilon)y^2 + 16(1+2\epsilon)y + 3(1+4\epsilon) + 4(1+2\epsilon)(2\Delta_{\text{ne}} - 1 - 2\epsilon)\cos 2\theta \\
&\quad + (1+4\epsilon)\cos 4\theta\} + 2\Omega_{\text{ne}}^2(1+3\epsilon)y\sin^4\theta, \\
B_{\text{ne}} &= (1+\epsilon)(y^2 - (1+2\epsilon)\cos^2\theta) + \Omega_{\text{ne}}\{(1+4\epsilon)y\cos^4\theta + y^2(y^3 - 3y^2 - (1+2\epsilon)(1+\sin^2\theta)) \\
&\quad + (1+2\epsilon)\cos^2\theta(2y^3 - y^2 + (1+2\epsilon)(1+\sin^2\theta))\} \\
&\quad + \Omega_{\text{ne}}^2(1+\epsilon)\sin^2\theta[y^2(3y^2 + 1 + 2\epsilon) + (1+2\epsilon)\cos^2\theta(y^2 - 1 - 2\epsilon)], \\
\Omega_{\text{ne}} &= \frac{2(1+\epsilon)y\sin\theta - (1-2q)\rho_{\text{ne}}^2\sqrt{\Delta_{\text{ne}}}}{\sin\theta[\rho_{\text{ne}}^2(y^2 + 1 + 2\epsilon) + 2(1+2\epsilon)y\sin^2\theta]}, \\
\Delta_{\text{ne}} &= y^2 - 2y + 1 + 2\epsilon, \\
\rho_{\text{ne}}^2 &= y^2 + \cos^2\theta + 2\epsilon\cos^2\theta,
\end{aligned} \tag{55}$$

where subscript “ne” stands for “near extremal.” For some constant  $\kappa$ , we can write

$$\begin{aligned}
(\Delta_{\text{ne}})^\kappa &\approx (y-1)^{2\kappa} \left[ 1 + \epsilon \frac{2\kappa}{(y-1)^2} \right], & \text{if } |y-1| \gg \epsilon \\
&\approx \epsilon^\kappa, & \text{otherwise,} \\
(\rho_{\text{ne}}^2)^\kappa &\approx (y^2 + \cos^2\theta)^\kappa \left[ 1 + \epsilon \frac{2\kappa\cos^2\theta}{y^2 + \cos^2\theta} \right], & \text{if } |y^2 + \cos^2\theta| \gg \epsilon \\
&\approx (\epsilon\cos^2\theta)^\kappa, & \text{otherwise.} \tag{56}
\end{aligned}$$

$y = 1$  was the location of the event horizon for an extremal black hole ( $a_* = 1$ ), which vanished as  $a_*$  was changed slightly from 1. As can be seen from the above expressions, this is a special point for  $\Delta_{\text{ne}}$ . For  $\rho_{\text{ne}}$ , the two cases correspond to being far from and near the ring singularity at  $r = 0, \theta = \pi/2$ , respectively.

As can be seen from Eq. (55),  $\Omega_{\text{ne}}$  is finite and smooth always (remember that at the pole, i.e., for  $\theta = 0$ , the only allowed value of  $\Omega$  is  $\Omega = 0$  and hence,  $\Omega_{\text{ne},\theta=0} = 0$ ). Therefore,  $A$  and  $B$  are also finite and smooth and we can restrict ourselves to studying  $\chi_{\text{ne}}$  to find any interesting sharp features in the radial profile of the modulus of the precession frequency  $\Omega_p$ , for a near-extremal NS. Indeed, we can see from  $\chi_{\text{ne}}$  given in Eq. (55) that the factor of  $\Delta_{\text{ne}}$  in the denominator will drive  $\Omega_p$  to rise sharply near  $y = 1$  for near-extremal naked singularities. The specific maxima/minima structure in the radial profile of  $\Omega_p$  can also be ascertained from Eq. (55).

### B. Near-extremal overspinning Kerr geometry and ultrahigh-energy collisions

Many interesting physical processes occur in near-extremal Kerr geometry at  $r = 1$  (in units of  $M$ ). These processes include ultrahigh-energy particle collisions and

collisional Penrose process with an extremely large efficiency of energy extraction.

In [21,22], we considered two particles which follow the geodesic motion on the equatorial plane of overspinning Kerr geometry starting from rest at infinity and undergo a collision at  $r = 1$ . One of the particles that is initially ingoing, turns back at radial coordinate  $0 < r < 1$  and appears at  $r = 1$  as an outgoing particle, while the second particle is ingoing. We showed that the center of mass energy of collision between the radially ingoing and outgoing particles shows divergence in the near-extremal limit where the Kerr spin parameter transcends the extremal value by an infinitesimal amount, i.e.,  $a = M(1 + \epsilon)$  with  $\epsilon \rightarrow 0^+$ . This process overcomes many limitations and fine-tunings involved in an analogous high-energy collision process between the two ingoing particles which occurs close to the event horizon of the maximally spinning BH [23,24].

We further showed that the particles which are produced in the ultrahigh-energy particle collisions in the overspinning Kerr spacetime can escape to infinity with divergent energies [25]. This is a consequence of the collisional Penrose process which allows us to extract rotational energy from the ergoregion of the Kerr spacetime. The efficiency of the collisional Penrose shows divergence in the near-extremal limit for the collisions which occur at  $r = 1$ , making it possible to extract a large amount of energy from the overspinning Kerr geometry. This is in stark contrast to the BH case, where efficiency is shown to be always finite with an upper bound of 14 [26]. Thus near-extremal NS spacetime can possibly be the source of the ultrahigh-energy cosmic rays and neutrinos.

Interestingly, as we showed earlier in this section, gyro precession frequency shows a sharp increase or decline close to  $r = 1$  in near-extremal overspinning Kerr spacetime as we decrease its radial coordinate along the constant value of  $\theta$ . This is precisely the location where

ultra-high-energy collisions and the collisional Penrose process with divergent efficiency occurs. Thus a thought experiment to the lower gyro which we described in this paper kills two birds with one stone. Firstly it allows us to identify the spacetime geometry which is conducive to the high-energy processes, as it can tell us whether the geometry is overspinning and near extremal. Secondly it also helps us to locate the region in space which can host high-energy processes, as gyro frequency exhibits a peculiar trend exactly at this location. This coincidence is quite remarkable.

## VII. FRAME-DRAGGING EFFECT IN ACCRETION DISKS IN A KERR GEOMETRY

In order to study the accretion disk around a spinning BH, one needs to study the stable circular orbits in the Kerr space-time. The last or innermost stable circular orbit (ISCO) marks the inner boundary of this disk. The ISCO radius depends on the Kerr parameter  $a_*$ , as shown in Fig. 7. This is a key underlying physical feature that can distinguish BHs from NSs, as we will see in this section.

The three fundamental frequencies for the accretion disk, namely, the Keplerian frequency  $\Omega_\phi$ , vertical epicyclic frequency  $\Omega_\theta$ , and the radial epicyclic frequency  $\Omega_r$ , are derived for the Kerr metric [27,28] (in geometrized units) as

$$\Omega_\phi = \pm \frac{M^{\frac{1}{2}}}{(r^{\frac{3}{2}} \pm aM^{\frac{1}{2}})} \quad (57)$$

$$\Omega_r = \Omega_\phi \left( 1 - \frac{6M}{r} \pm \frac{8aM^{\frac{1}{2}}}{r^{\frac{3}{2}}} - \frac{3a^2}{r^2} \right)^{\frac{1}{2}} \quad (58)$$

$$\Omega_\theta = \Omega_\phi \left( 1 \mp \frac{4aM^{\frac{1}{2}}}{r^{\frac{3}{2}}} + \frac{3a^2}{r^2} \right)^{\frac{1}{2}}, \quad (59)$$

where the upper sign is applicable for a direct orbit and the lower one for a retrograde orbit. These frequencies are related to the precession of the orbit and orbital plane. Precession of the orbit is measured by the periastron precession frequency ( $\Omega_{\text{per}}$ ), and orbital plane precession is measured by the nodal plane precession or Lense-Thirring precession frequency ( $\Omega_{\text{nod}}$ ) [29]. These two frequencies are defined as [30]

$$\Omega_{\text{per}} = \Omega_\phi - \Omega_r, \quad (60)$$

$$\Omega_{\text{nod}} = \Omega_\phi - \Omega_\theta. \quad (61)$$

Orbital plane precession arises only due to the rotation of the spacetime. In a nonrotating spacetime,  $\Omega_\phi$  is always equal to  $\Omega_\theta$ , and hence the Lense-Thirring precession is entirely absent. However, periastron precession occurs both in rotating and nonrotating spacetimes. We note that the square of the radial epicyclic frequency  $\Omega_r^2$  vanishes at the ISCO and is negative for smaller radii, which shows a radial instability for such orbits. Outside the ISCO,  $\Omega_r^2$  is always positive and  $\Omega_\theta^2$  is always nonzero and positive in a rotating spacetime. The same cannot be said about  $\Omega_{\text{nod}}$ . For example, the LT precession frequency [Eq. (61)] can be zero at  $r = r_0$ , given by

$$\Omega_{\text{nod}}(r_0) = 0 \Rightarrow r_0 = \frac{9}{16} a_*^2 M = 0.5625 a_*^2 M. \quad (62)$$

Since  $r_0$  is always less than  $r_{\text{ISCO}}$  ( $6M \geq r_{\text{ISCO}} \geq M$  [15]) and even inside the event horizon for a BH ( $0 \leq a_* \leq 1$ ), the LT precession frequency never becomes zero for a BH spacetime. We now discuss the location of the ISCO in a NS spacetime and argue that its relation with  $r_0$  has implications for distinguishing BH and NS spacetimes.

Figure 7 shows that the ISCO radius decreases with increasing  $a_*$  for prograde orbits for both BHs and NSs up to  $a_* = \sqrt{32/27} \approx 1.089$ , and then increases [31–33]. Therefore, the minimum ISCO radius, having the value  $r_{\text{ISCO}} = 2M/3$ , occurs for  $a_* = 1.089$ . As seen from Fig. 7, the ISCO lies on or inside the ergosurface for  $0.943 \leq a_* \leq 2.838$ . For each  $a_*$  value, there exists a radius ( $r_0$ ) at which there is no frame-dragging effect, and hence the LT precession vanishes. This radius is less than the ISCO radius for  $a_* < 1.089$  (Fig. 7), but this may not be observationally important, as the accretion disk extends up

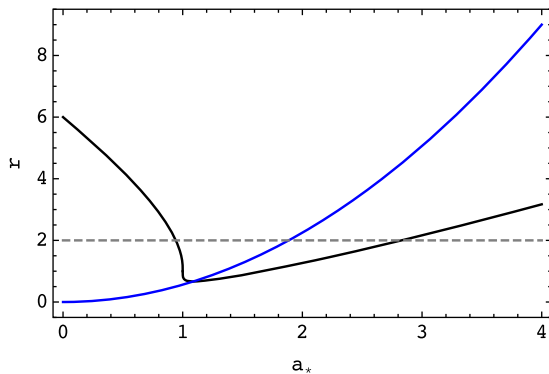


FIG. 7. Three radial quantities (in units of  $M$ ) for prograde orbits, namely, the ISCO radius (black), the ergoradius (dashed gray), and the radius ( $r_0$ ) at which the precession frequency ( $\Omega_{\text{nod}}$ ) vanishes (blue curve), plotted as functions of the dimensionless Kerr parameter  $a_* = a/M$ . The ISCO radius lies outside the ergoregion for all  $a_*$  except  $0.943 \leq a_* \leq 2.838$ .  $r_0$  meets the ISCO radius at  $a_* = 1.089$ . This has the implication that for smaller values of  $a_*$ , the LT frequency is always positive and does not vanish for any radius. For larger values, there is a domain of  $r$  for which this frequency becomes negative, signifying that the LT effect switches sign. Since this feature is exhibited for  $a_* = 1.089 > 1$ , the LT frequency in a BH spacetime never vanishes. We point out that NSs with  $a_* < 1.089$  also do not display vanishing LT frequency.

to  $r_{\text{ISCO}}$ . Figure 7 also shows that  $r_0$  equals  $r_{\text{ISCO}}$  for  $a_* = 1.089$  [34] and is greater than  $r_{\text{ISCO}}$  for  $a_* > 1.089$ . These make 1.089 a special value of  $a_*$ .

In the case of BHs, the LT frequency increases with decreasing  $r$  up to the inner edge of the accretion disk [see Figs. 8 and 9(a)]. But for NSs, the LT frequency attains a maximum at  $r = r_p$  which occurs always at  $r(r = r_p) > r_{\text{ISCO}}$  (see Table I), and then decreases as  $r$  decreases [Figs. 8 and 9(b)]. As shown in Figs. 7, 8, and 9(b), the LT precession frequency becomes negative for  $r_{\text{ISCO}} \leq r < r_0$ , in the case of  $a_* > 1.089$ . This means that the direction of LT precession is reversed. The maximum value of  $\Omega_{\text{nod}}$  ( $=1/2M$ ) occurs for  $a_* = 1$  at  $r = r_{\text{ISCO}}$ . We also note that

$$\left. \frac{d\Omega_{\text{nod}}}{dr} \right|_{r_{\text{ISCO}}} < 0 \quad \text{for BH,} \quad (63)$$

$$\left. \frac{d\Omega_{\text{nod}}}{dr} \right|_{r_{\text{ISCO}}} > 0 \quad \text{for NS,} \quad (64)$$

and hence  $\Omega_{\text{nod}}$  decreases (increases) with  $r$  at  $r_{\text{ISCO}}$  for BHs (NSs).

The profiles of the other frequencies, i.e.,  $\Omega_\phi$ ,  $\Omega_r$ ,  $\Omega_\theta$ , and  $\Omega_{\text{per}}$ , can also show differences between BHs and NSs. Figure 10 shows that  $\Omega_\phi$  behaves similarly for BHs and

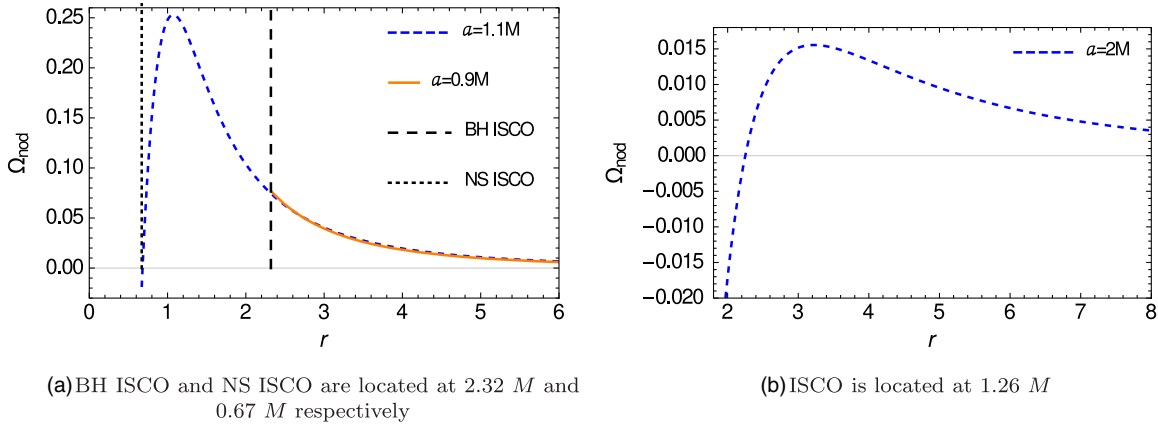


FIG. 8. Variation of  $\Omega_{\text{nod}}$  (in units of  $M^{-1}$ ) versus  $r$  (in units of  $M$ ). It is seen from the plots that the nodal plane precession frequency  $\Omega_{\text{nod}}$  always increases as one approaches a BH but in the case of a NS, we obtain a peak value of  $\Omega_{\text{nod}}$  for all  $a_* > 1$ .  $\Omega_{\text{nod}}$  vanishes in a particular orbit of radius  $r_0$  for  $a_* \geq 1.089$  and it becomes negative (which means that the LT precession reverses direction) in all the orbits which are in the range  $r_0 > r \geq r_{\text{ISCO}}$  for  $a_* > 1.089$ .

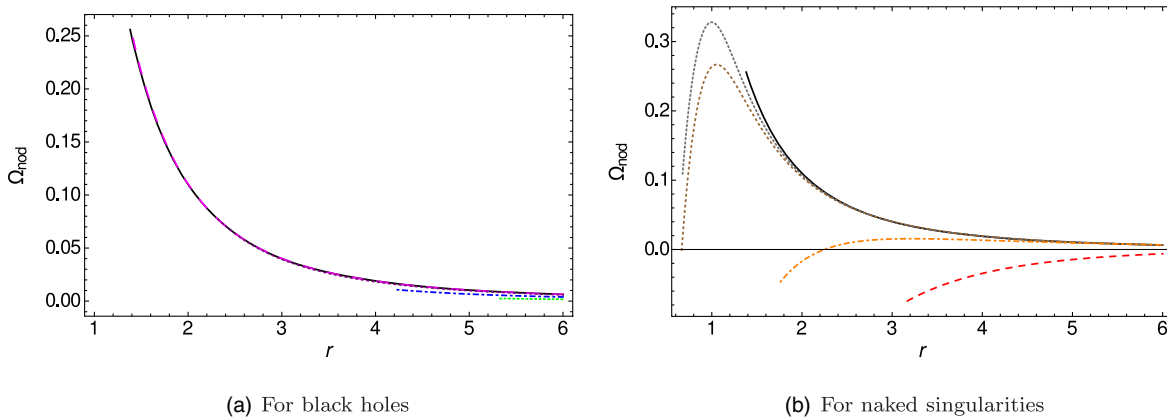


FIG. 9. We show the radial variation of the precession frequency ( $\Omega_{\text{nod}}$ ) (in units of  $M^{-1}$ ) for different  $a_*$  BHs in the left panel and NSs on the right panel. For BHs, we plot  $\Omega_{\text{nod}}$  between their respective ISCO radii and  $r = 6$ . We have used  $a_* = 1$  (black), 0.9999 (magenta dashed), 0.9 (purple dotted), 0.5 (blue dotted-dashed), and 0.2 (green dashed curve).  $\Omega_p$  decreases with increasing  $r$  always for BHs. For NSs, we plot  $\Omega_{\text{nod}}$  between their respective ISCO radii and  $r = 6$ . We have included also the extremal BH case to demonstrate the clear change in characteristic features. We have used  $a_* = 1$  (black), 1.05 (gray dashed), 1.089 (brown dotted), 2 (orange dotted-dashed), and 4 (red dashed curve). For NSs, as we increase  $r$ ,  $\Omega_{\text{nod}}$  always increases initially at the ISCO radius, reaches a peak value and decreases. Negative  $\Omega_{\text{nod}}$  implies that the sense of precession has changed. These are characteristic features of NSs.

TABLE I. An object of mass  $M = 10 M_{\odot}$  ( $=15$  km) has been considered to calculate  $\nu_{\phi}$  (Kepler frequency),  $\nu_{\theta}$  (vertical epicyclic frequency), and  $\nu_{\text{nod}}$  (nodal plane precession frequency) using Eqs. (57) and (59). For an example, the conversion factor between  $\nu_{\phi}$  and  $\Omega_{\phi}$  is as follows:  $\nu_{\phi}$  (in kHz) =  $\Omega_{\phi}$  (in  $\text{km}^{-1} \times \frac{300}{2\pi}$ ), and so on. For other values of  $M$ , the values of  $\nu_{\phi}$ ,  $\nu_{\theta}$ ,  $\nu_{\text{nod}}$  (columns 3, 4, 5, and 6) of the table have to be multiplied by  $10 M_{\odot}/M$ . The values in the parentheses of column 6 show the position of the peak of  $\nu_{\text{nod}}$ .

$a_*$	$r_{\text{ISCO}}$ ( $M$ )	$\nu_{\phi}$ (Hz)	$\nu_{\theta}$ (Hz)	$\nu_{\text{nod}}$ at $r_{\text{ISCO}}$ (Hz)	$\nu_{\text{nod}}$ (Hz) at $r_p$ (mentioned in parentheses)
0.1	5.67	234	231	3	Not applicable
0.2	5.32	255	247	8	Not applicable
0.3	4.98	279	265	14	Not applicable
0.4	4.61	309	287	22	Not applicable
0.5	4.23	346	312	34	Not applicable
0.6	3.82	395	342	53	Not applicable
0.7	3.39	458	378	80	Not applicable
0.8	2.91	552	421	131	Not applicable
0.9	2.32	718	472	246	Not applicable
0.98	1.61	1053	462	590	Not applicable
0.99	1.45	1163	420	743	Not applicable
0.999	1.18	1395	252	1142	Not applicable
0.9999	1.07	1510	118	1392	Not applicable
0.99999	1.03	1556	54	1502	Not applicable
0.999999	1.016	1572	30	1542	Not applicable
1.0	1	1591	0	1591	Not applicable
1.000001	0.98	1615	40	1575	1586 (0.998)
1.00001	0.96	1640	84	1556	1584 (0.994)
1.0001	0.93	1677	157	1520	1571 (0.992)
1.001	0.86	1769	370	1399	1528 (0.976)
1.01	0.75	1918	900	1017	1367 (0.952)
1.02	0.71	1967	1199	768	1261 (0.962)
1.04	0.68	1988	1538	450	1104 (0.976)
1.06	0.67	1979	1745	234	1004 (0.984)
1.08	0.667	1959	1894	65	886 (1.04)
$\sqrt{32/27} \approx 1.089$	2/3	1949	1949	0	847 (1.05)
1.1	0.67	1935	2013	-77	804 (1.07)
2	1.26	932	1588	-655	49 (3.2)
4	3.17	330	566	-236	2 (12.3)
6	5.38	172	288	-116	0.25 (27.7)

NSs, but much larger values are possible for the latter, simply because the disk can extend up to much lower radii. Figure 11 shows that a small additional peak appears in the plot of the  $\Omega_r$  profile for the near-extremal value of  $a_*$  in the case of a NS. Such a peak appears at small radius values, where an accretion disk cannot exist in the case of a BH. As  $a_*$  increases, this peak becomes more prominent for  $a_* = 1.01$  and it becomes the only peak for  $a_* \sim 1.05$ . Such an additional peak does not appear for the case of a BH. Similarly, a minimum occurs in the  $\Omega_{\theta}$  profiles for NSs with  $1 < a_* < 1.1$  near the radius  $r = M$  (Fig. 12). Such a minimum does not occur for a BH. Besides,  $\Omega_{\theta}$  for  $a_*$  roughly above 1.01 can attain a much higher value than that for BHs. Finally, the periastron precession frequencies for NSs can attain values much higher than those for BHs (Fig. 13).

### A. Observational aspects

BH x-ray binary (BHXB) sources show a plethora of timing features in x rays [30]. Most notable among them are high-frequency (HF) QPOs and three types of low-frequency (LF) QPOs. Sometimes two HF QPOs are seen together. Their frequencies are observed to be in the range of several tens to several hundreds of hertz. For example, while XTE 1650-500 has shown HF QPOs in the range of 50–270 Hz, 4U 1630-47 has shown such QPOs in the range of 150–450 Hz [35]. The three LF QPOs are denoted with types A, B, and C, and their frequencies are typically in the ranges 6.5–8 Hz, 0.8–6.4 Hz, and 0.01–30 Hz respectively. While several models exist to explain these QPOs, they are often associated with the relativistic precession (RP) of the accretion disk, and hence with the frequencies  $\Omega_{\phi}$ ,  $\Omega_r$ ,  $\Omega_{\theta}$ ,  $\Omega_{\text{per}}$ , and  $\Omega_{\text{nod}}$ .

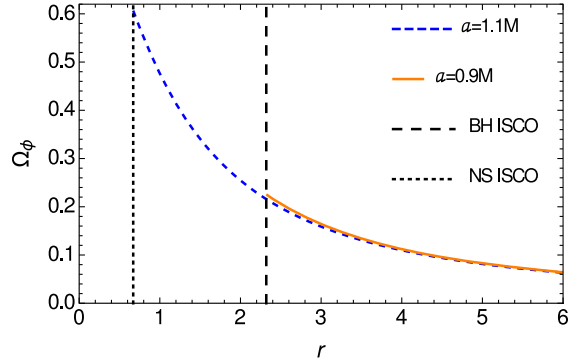


FIG. 10. Variation of  $\Omega_\phi$  (in units of  $M^{-1}$ ) versus  $r$  (in units of  $M$ ). The BH ISCO and NS ISCO are located at  $2.32M$  and  $0.67M$ , respectively. The plots show that the Kepler frequency  $\Omega_\phi$  for a NS is much higher than that for a BH at the respective ISCOs for  $\epsilon = \pm 0.1$ , i.e.,  $a_* = 0.9$  and  $a_* = 1.1$ . The difference between the values of Kepler frequencies of a NS and a BH decreases with decreasing the value of  $\epsilon$ .

The RP model was originally conceived to explain the twin kilohertz QPOs and a low-frequency QPO of neutron star low-mass x-ray binaries [36,37]. Following this idea, frequencies of the C-type LF QPO, the lower-frequency

HF QPO and the higher-frequency HF QPO of BHXBs are identified with  $\Omega_{\text{nod}}$ ,  $\Omega_{\text{per}}$ , and  $\Omega_\phi$  respectively [38]. This can be useful to measure both the mass ( $M$ ) and  $a_*$  of the compact object, as demonstrated by [39]. Table I shows that the observed LF QPOs could be identified with  $\Omega_{\text{nod}}$  only for  $a_* < 0.5$  and  $a_* \sim 1.089$  (see also [40]). In fact,  $\Omega_{\text{nod}}$  could have a much higher value for  $a_*$ , closer to 1 for both BH and NS, and it could be possible to identify a HF QPO with  $\Omega_{\text{nod}}$  (Table I). If  $a_*$  is very close to 1, the  $\Omega_{\text{nod}}$  value is quite high (Table I), and such high-frequency QPOs could be detected in the future for BHs and NSs with  $a_* \approx 1$ . While there are uncertainties in the specific identifications of observed frequencies with the theoretical ones, the recent discovery of the C-type quasiperiodic variation of the broad relativistic spectral iron line energy from the BHXB H1743-322 strongly suggests that the inner accretion disk of this source is indeed tilted and precessing [41]. Therefore, the theoretical dependencies of various frequencies on  $a_*$ , as discussed in this section, have the potential to distinguish between a BH and a NS.

How could this be done? Here we give some examples. Note that most of the BHXBs are transient sources, and an accretion disk is formed only during an outburst. Even for the persistent BHXBs, the source state often changes,

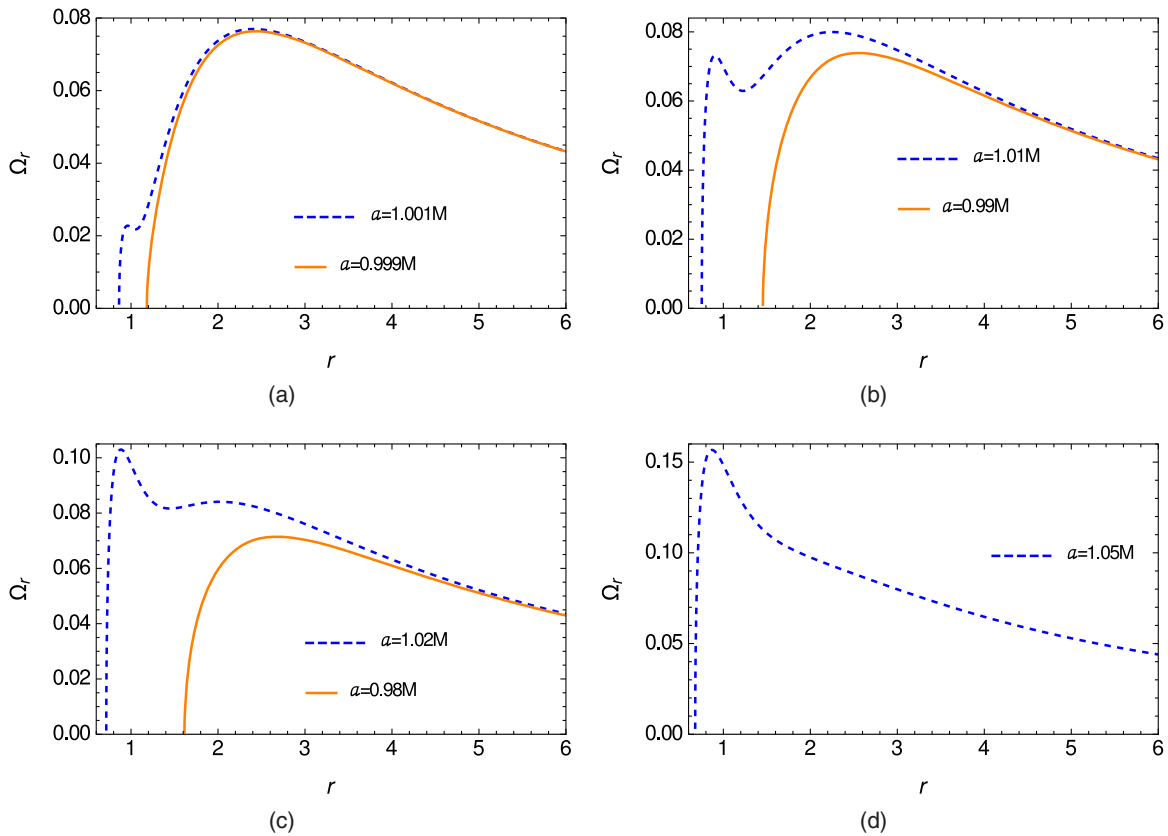
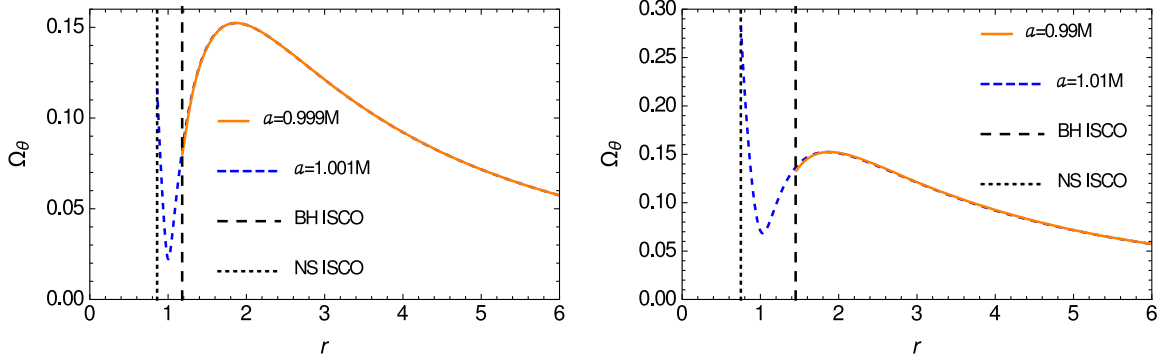
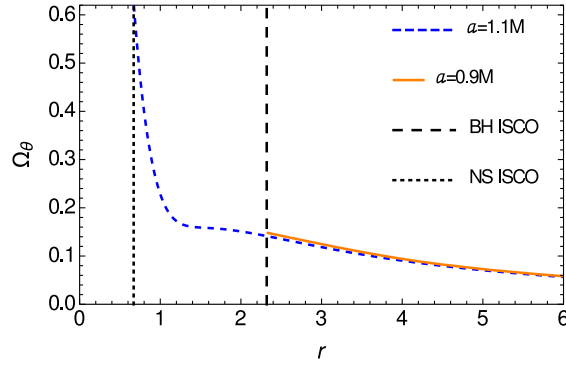


FIG. 11. Variation of  $\Omega_r$  (in units of  $M^{-1}$ ) versus  $r$  (in units of  $M$ ). The plots show that  $\Omega_r$  vanishes at the respective ISCOs of a BH and a NS, which is expected, but it can be seen that a small “kink” appears in some of these near-extremal NS cases. This feature is quite clear for  $a_* \gtrsim 1.001$  and it disappears for  $a_* = 1.05$ .



(a) BH ISCO and NS ISCO are located at  $1.18 M$  and  $0.86 M$  respectively

(b) BH ISCO and NS ISCO are located at  $1.45 M$  and  $0.75 M$  respectively



(c) BH ISCO and NS ISCO are located at  $2.32 M$  and  $0.67 M$  respectively

FIG. 12. Variation of  $\Omega_\theta$  (in units of  $M^{-1}$ ) versus  $r$  (in units of  $M$ ). The plots show that a local minimum always appears outside of the ISCO for  $1 < a_* < 1.1$  in  $\Omega_\theta$  curves, in principle. This feature is completely absent in the case of a BH.

which implies changes in accretion components. So it is expected that the accretion disk of a given BHXB sometimes advances towards the central object and sometimes recedes, depending on the source intensity and spectral states. If QPOs are connected to the natural frequencies

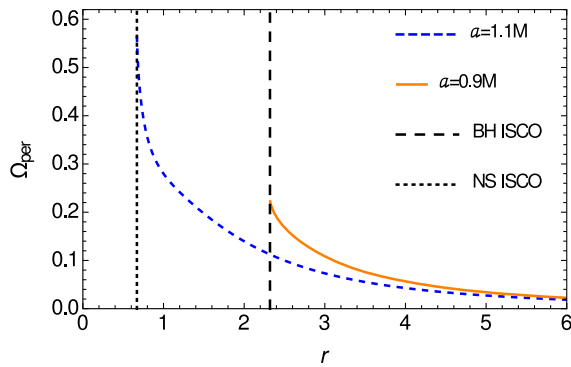


FIG. 13. Comparison between the periastron precession frequencies ( $\Omega_{\text{per}}$  in units of  $M^{-1}$ ) of a BH and a NS at their respective ISCOs for  $\epsilon = \pm 0.1$ . The BH ISCO and NS ISCO are located at  $2.32M$  and  $0.67M$ , respectively.

mentioned above, then such a dynamics of the disk would mean changes in QPO frequencies, as these frequencies depend on the radial distance. And we do observe evolution of QPO frequencies. As a BH and a NS have significantly different theoretical radial profiles of frequencies, it could be, in principle, possible to distinguish them by tracking the evolution of QPO frequencies as the disk advances or recedes. For example,  $\Omega_{\text{nod}}$  for a BH will monotonically increase, and will attain the maximum value, if the disk advances up to the ISCO radius. But  $\Omega_{\text{nod}}$  for a NS will first increase, will attain the maximum value, and then will decrease, as the disk advances up to  $r_{\text{ISCO}}$ , which can be quite different from the  $r_{\text{ISCO}}$  of a BH. In fact, in the case of a NS, the absolute value of  $\Omega_{\text{nod}}$  can become zero and then increase again. Whether this will happen and what the radial locations of the maximum and zero values of  $\Omega_{\text{nod}}$  are depend on  $a_*$ . Therefore, the Lense-Thirring precession can provide a way to distinguish between a BH and a NS. Similarly, the maximum possible value of  $\Omega_\phi$  depends on  $a_*$ . Finally, according to the above-mentioned model,  $\Omega_r$  is interpreted as the separation between two HF QPO frequencies. Therefore, the qualitatively different  $\Omega_r$  radial

profiles for NSs with  $a_* \lesssim 1.05$  can be useful to distinguish them from BHs.

### VIII. CONCLUSION

The precession frequencies of the spin of test gyros attached to timelike stationary observers in the BH case are finite both in and outside of the ergoregion but become arbitrarily large as one considers a gyro located in an orbit close to the horizon,  $r \sim r_+$ , in any direction ( $0 < \theta \leq \pi/2$ ). In contrast to this, for a NS, the precession frequencies of such gyros remain finite and regular even if one considers those close to  $r = 0$ , for all  $\theta \approx \pi/2$ . Since the ring singularity itself is present at  $r = 0$ ,  $\theta = \pi/2$ , the gyro frequency diverges in the limit of the approach to this region. For gyros placed increasingly closer to a BH or NS in the equatorial plane, their precession frequencies diverge in both cases in different ways; that is, the frequencies diverge close to the horizon in the case of a BH, whereas the divergence occurs close to  $r = 0$  for a NS.

Interestingly, we have shown that the spin precession frequency stays finite in the limit of the approach to the horizon for a ZAMO ( $q = 0.5$ ) and diverges in all other cases. Further, we have shown that a sharp rise/fall in the modulus of the precession frequency is a tell-tale indication of the existence of a near-extremal naked singularity, and the location of this feature is at  $r = 1$ . The specific maxima/minima structure in the radial profile of the modulus of the precession frequency  $\Omega_p$  for a near-extremal naked singularity (for example, two local maxima or two local minima, two peaks or three peaks with a plateau, etc.) would indicate how fast the observer is moving with respect to the ZAMO frequency.

As we find, the nodal plane precession frequency, related to the accretion disc, has distinctive features that can be used to characterize both black holes and naked singularities, and we summarize them here. We can use these features to potentially make a statement regarding the existence of a NS: (i) A maximum or a peak is obtained for  $\Omega_{\text{nod}}$  at some  $r = r_p(a_*)$  for all  $a_* > 1$ , indicating the existence of a NS. (ii)  $\Omega_{\text{nod}}$  vanishes at  $r = r_0$  for a NS with  $a_* \geq 1.089$  and becomes negative (which means that the LT precession reverses direction) in all orbits with  $r_0 > r \geq r_{\text{ISCO}}$ , for a NS with  $a_* > 1.089$ . (iii) Additionally,  $\Omega_{\text{nod}}$  shows a peculiar effect:  $\Omega_{\text{nod}} \propto r^n$  (where  $n \gtrsim 0$ ; see Fig. 8) in the region  $r_0 \leq r < r_p$ . This curve does not follow the inverse cube law of distance like other astrophysical objects. All these features are completely absent in the case of a BH and this would be reflected in the observation of frequencies of QPOs.

Finally, it can be seen from Figs. 11 and 12 that  $\Omega_r$  and  $\Omega_\theta$  also have characteristic differences [42] in the cases of a BH and a NS by which it may be possible to detect a NS if  $\Omega_r$  and  $\Omega_\theta$  are the observationally measurable quantities [43]. It follows that if all of the above-mentioned features are never observed, then we can conclusively state that Kerr naked singularities do not exist, or at least their abundance may be extremely small.

### ACKNOWLEDGMENTS

We thank the referee for the valuable comments and suggestions. M. P. acknowledges support from the Narodowe Centrum Nauki (NCN) grant Harmonia 6 (UMO2014/14/M/ST9/00707).

- 
- [1] <http://www.eventhorizontelescope.org/>.
- [2] C. Chakraborty and P. Majumdar, *Classical Quantum Gravity* **31**, 075006 (2014).
- [3] C. Chakraborty, P. Kocherlakota, and P. S. Joshi, *Phys. Rev. D* **95**, 044006 (2017).
- [4] P. S. Joshi, D. Malafarina, and R. Narayan, *Classical Quantum Gravity* **31**, 015002 (2014).
- [5] D. Bini, A. Geralico, and R. T. Jantzen, *Phys. Rev. D* **94**, 064066 (2016).
- [6] D. Bini, A. Geralico, and R. T. Jantzen, *Phys. Rev. D* **94**, 124002 (2016).
- [7] S. A. Hojman and F. A. Asenjo, *Classical Quantum Gravity* **30**, 025008 (2013).
- [8] C. Armaza, M. Banados, and B. Koch, *Classical Quantum Gravity* **33**, 105014 (2016).
- [9] C. W. Misner, K. S. Thorne, and J. A. Wheeler, *Gravitation* (W. H. Freeman & Company, San Francisco, 1973).
- [10] N. Straumann, *General Relativity with Applications to Astrophysics* (Springer, Berlin, 2009).
- [11] R. T. Jantzen, P. Carini, and D. Bini, *Ann. Phys. (N.Y.)* **215**, 1 (1992).
- [12] C. Chakraborty, K. P. Modak, and D. Bandyopadhyay, *Astrophys. J.* **790**, 2 (2014).
- [13] D. Chatterjee, C. Chakraborty, and D. Bandyopadhyay, *J. Cosmol. Astropart. Phys.* **01** (2017) 062.
- [14] J. M. Bardeen, *Astrophys. J.* **162**, 71 (1970).
- [15] J. M. Bardeen, W. H. Press, and S. A. Teukolsky, *Astrophys. J.* **178**, 347 (1972).
- [16] E. G. Gimon and P. Horava, *Phys. Lett. B* **672**, 299 (2009).
- [17] J. B. Hartle, *Gravity: An Introduction to Einstein's General Relativity* (Pearson, San Francisco, 2003).
- [18] K. Sakina and J. Chiba, *Phys. Rev. D* **19**, 2280 (1979).
- [19] D. Malafarina and P. S. Joshi, [arXiv:1603.02848v1](https://arxiv.org/abs/1603.02848v1).

- [20] Z. Li and C. Bambi, *J. Cosmol. Astropart. Phys.* **03** (2013) 031.
- [21] M. Patil and P. S. Joshi, *Classical Quantum Gravity* **28**, 235012 (2011).
- [22] M. Patil and P. S. Joshi, *Phys. Rev. D* **84**, 104001 (2011).
- [23] M. Banados, J. Silk, and S. West, *Phys. Rev. Lett.* **103**, 111102 (2009).
- [24] T. Harada and M. Kimura, *Classical Quantum Gravity* **31**, 243001 (2014).
- [25] M. Patil, T. Harada, K. Nakao, P. S. Joshi, and M. Kimura, *Phys. Rev. D* **93**, 104015 (2016).
- [26] J. Schnittman, *Phys. Rev. Lett.* **113**, 261102 (2014).
- [27] A. T. Okazaki, S. Kato, and J. Fukue, *Publ. Astron. Soc. Jpn.* **39**, 457 (1987).
- [28] S. Kato, *Publ. Astron. Soc. Jpn.* **42**, 99 (1990).
- [29] J. Lense and H. Thirring, *Phys. Z.* **19**, 156 (1918).
- [30] T. M. Belloni and L. Stella, *Space Sci. Rev.* **183**, 43 (2014).
- [31] Z. Stuchlík, *Bull. Astron. Inst. Czech.* **31**, 129 (1980).
- [32] D. Pugliese, H. Quevedo, and R. Ruffini, *Phys. Rev. D* **84**, 044030 (2011).
- [33] I. F. Ranea-Sandoval and H. Vucetich, *Relativity and Gravitation* **157**, 435 (2014).
- [34] S. Chandrasekhar, *The Mathematical Theory of Black Holes* (Oxford, New York, 1992).
- [35] T. Belloni, A. Sanna, and M. Méndez, *Mon. Not. R. Astron. Soc.* **426**, 1701 (2012).
- [36] L. Stella and M. Vietri, *Astrophys. J.* **492**, L59 (1998).
- [37] L. Stella and M. Vietri, *Phys. Rev. Lett.* **82**, 17 (1999).
- [38] A. Ingram and S. Motta, *Mon. Not. R. Astron. Soc.* **444**, 2065 (2014).
- [39] S. E. Motta, T. M. Belloni, L. Stella, T. Munoz-Darias, and R. Fender, *Mon. Not. R. Astron. Soc.* **437**, 2554 (2014); **439**, L65 (2014).
- [40] L. Stella and A. Possenti, *Space Sci. Rev.* **148**, 105 (2009).
- [41] A. Ingram, M. van der Klis, M. Middleton, C. Done, D. Altamirano, L. Heil, P. Uttley, and M. Axelsson, *Mon. Not. R. Astron. Soc.* **461**, 1967 (2016).
- [42] G. Török and Z. Stuchlík, *Astron. Astrophys.* **437**, 775 (2005).
- [43] Z. Stuchlík and J. Schee, *Classical Quantum Gravity* **29**, 065002 (2012).